

IMPROVING THE PERFORMANCE OF NICKEL OXIDE-BASED
MAPbI₃ PEROVSKITE SOLAR CELLS

BAUKE STEENSMA



Prof. Dr. M.A. Loi
B.G.H.M. Groeneveld, MSc

May 2017

This thesis is submitted as required for the completion of the degree of *MSc Applied Physics* at the University of Groningen

DETAILS:

Author – Bauke Steensma

Student number – s2029227

Group – Photophysics and OptoElectronics

SUPERVISORS:

Prof. Dr. M.A. Loi

B.G.H.M. Groeneveld, MSc



university of
 groningen

faculty of science
 and engineering

ABSTRACT

In this thesis perovskite solar cells are investigated with an active layer of MAPbI_3 and a HTL of NiO. The inorganic NiO was chosen since it is more stable (in air) than organic HTLs, and leads to a higher V_{oc} . Furthermore both MAPbI_3 and NiO are solution processable, which allows for upscaling, and therefore a reduction in the production costs. Two device structures were studied, where the ETL was varied between PTEG-1 and PCBM. The solvent used to process this layer was varied between chlorobenzene and chloroform. Overall the devices made with PTEG-1 achieved about 3% higher power conversion efficiencies, with the champion cell reaching 17.7%. The change of ETL from PCBM to PTEG-1 resulted in a J_{sc} of up to 23 mA/cm^2 , an increase of nearly 3 mA/cm^2 , while further slightly improving the V_{oc} from 1.05 V to 1.1 V. The increase of J_{sc} and V_{oc} can possibly be explained by the reduction of trap-assisted recombination at the perovskite-ETL interface. Both device structures show a severe light soaking effect, and have inconsistent fill factors, reaching anywhere from 35% to 70%. Changing the solvent for PTEG-1 from chlorobenzene to chloroform reduced the light soaking effect significantly, possibly due to an improved morphology. The addition of the ternary solvent NMP to the perovskite solution combined with an anti-solvent treatment, was investigated in order to improve the fill factor of the devices. The morphology improved considerably, allowing for fill factors up to 73%: the highest in this thesis. Unfortunately the J_{sc} and V_{oc} were reduced due to thinner MAPbI_3 films. Next, three different precursors for the NiO were explored. The thickness and morphology of the NiO layers were subsequently studied, aiming at improving the NiO layer. Finally a qualitative experiment is presented, which discusses the influence and necessity of scrubbing of the ITO anodic contacts.

*Accept yourself, love yourself, and keep moving forward.
If you want to fly, you have to give up what weighs you down.*

— Roy T. Bennett

ACKNOWLEDGEMENTS

I would like to thank everybody from the Photophysics and OptoElectronics group: without them I would not have produced this thesis, nor would I have had such a great time during my research. In particular I would like to express my gratitude to

Professor Maria A. Loi – For giving me the opportunity to carry out my master research in her group, helping me find an internship, as well as giving me advice.

B.G.H.M. Groeneveld, MSc – Teaching me most of the experimental techniques and equipment, always being available for questions, giving excellent feedback and guidance, and being an amazing supervisor overall.

Teodor Zaharia – For carrying out the ellipsometry measurements, and being great help overall as a technician.

Arjen Kamp – For giving the general trainings in the cleanrooms and for troubleshooting in my office and the labs.

M. Salverda, MSc – Helping Bart and me out with x-ray reflectivity measurements.

Xinkai Qiu – For training me in the atomic force microscope.

CONTENTS

| | | |
|-----------|--|-----------|
| I | BACKGROUND INFORMATION | 1 |
| 1 | INTRODUCTION | 3 |
| 2 | THEORY | 5 |
| 2.1 | Hybrid inorganic-organic perovskites | 5 |
| 2.2 | Photovoltaic operation | 5 |
| 2.2.1 | Ohmic contact | 6 |
| 2.2.2 | Charge separation | 8 |
| 2.3 | Solar cell characterization | 10 |
| 2.4 | Energy loss mechanisms | 12 |
| 2.4.1 | Recombination | 12 |
| 2.4.2 | Bandgap losses | 13 |
| 2.5 | Undesirable behavior | 14 |
| 2.5.1 | Hysteretic behavior | 14 |
| 2.5.2 | Light soaking phenomenon | 16 |
| 3 | MATERIAL PROPERTIES | 19 |
| 3.1 | ITO substrates | 19 |
| 3.2 | NiO | 20 |
| 3.3 | MAPbI ₃ | 20 |
| 3.4 | PC ₆₀ BM | 21 |
| 3.5 | PTEG-1 | 22 |
| 3.6 | Aluminum | 22 |
| II | EXPERIMENTAL METHODS | 23 |
| 4 | DEVICE FABRICATION | 25 |
| 4.1 | Solution preparation | 25 |
| 4.1.1 | Nickel oxide precursor solution | 25 |
| 4.1.2 | MAPbI ₃ solution | 26 |
| 4.1.3 | PCBM and PTEG-1 solutions | 26 |
| 4.2 | Substrate preparation | 26 |
| 4.3 | Spincoating and annealing procedures | 27 |
| 4.3.1 | NiO procedure | 28 |
| 4.3.2 | MAPbI ₃ procedure | 29 |
| 4.3.3 | PCBM and PTEG-1 procedure | 29 |
| 4.4 | Thermal evaporation of aluminum top contacts | 30 |
| 5 | MEASUREMENT TECHNIQUES | 31 |
| 5.1 | J-V measurements | 31 |
| 5.2 | EQE measurements | 32 |
| 5.3 | Thickness measurements | 33 |
| 5.3.1 | Dektak | 33 |
| 5.3.2 | XRR | 33 |
| 5.3.3 | Ellipsometer | 34 |
| 5.4 | Optical microscope | 34 |

| | | |
|------------|--|-----------|
| 5.5 | AFM measurements | 34 |
| 6 | INFLUENCE OF ITO SCRUBBING METHOD | 37 |
| 6.1 | Different scrubbing methods | 38 |
| III | EXPERIMENTS, RESULTS AND DISCUSSION | 41 |
| 7 | NICKEL OXIDE THIN FILM CHARACTERIZATION | 43 |
| 7.1 | Thickness measurements | 44 |
| 7.2 | Microscopy measurements | 45 |
| 8 | COMPARING ETLs: PCBM VS. PTEG-1 | 47 |
| 8.1 | Layer Thickness | 47 |
| 8.2 | Device performance | 47 |
| 8.3 | Light soaking | 50 |
| 9 | ETL SOLVENT: CHLOROBENZENE VS. CHLOROFORM | 53 |
| 9.1 | Device performance | 53 |
| 9.2 | Light soaking | 53 |
| 10 | ANTI-SOLVENT TREATMENT OF MAPBI ₃ | 55 |
| 10.1 | Ternary solvent | 55 |
| 10.2 | Anti-solvent treatment: two-step spincoating | 56 |
| 10.3 | Varying the spincoating parameters | 56 |
| 11 | CONCLUSIONS AND OUTLOOK | 59 |
| | BIBLIOGRAPHY | 63 |

LIST OF FIGURES

| | | |
|-----------|---|----|
| Figure 1 | Perovskite structure. | 6 |
| Figure 2 | Ohmic contact energy bands. | 7 |
| Figure 3 | PN junction unbiased. | 9 |
| Figure 4 | Biased PN junctions. | 10 |
| Figure 5 | J-V curve. | 11 |
| Figure 6 | Equivalent circuits of solar cells. | 12 |
| Figure 7 | R_s and R_{sh} influence on J-V curve. | 13 |
| Figure 8 | Solar spectrum AM0, AM1.5, and BB at 6000K. | 14 |
| Figure 9 | Hysteretic J-V behavior. | 15 |
| Figure 10 | Iodine diffusion in MAPbI ₃ and PL of a thin MAPbI ₃ film. | 17 |
| Figure 11 | Structure of PCBM and PTEG-1. | 19 |
| Figure 12 | Energy band diagram of used materials. | 20 |
| Figure 13 | (Un)scrubbed ITO substrate by hand. | 37 |
| Figure 14 | (Un)scrubbed ITO substrate with diamond lap- ping paper. | 38 |
| Figure 15 | Scrubbed ITO substrates with diamond lap- ping paper of 0.5 micrometer and steel wool. | 39 |
| Figure 16 | (Un)scrubbed FTO substrate by hand. | 39 |
| Figure 17 | NiO thin film thickness determination. | 43 |
| Figure 18 | Optical microscope nickel nitrate 4000 rpm. | 45 |
| Figure 19 | AFM measurements of NiO films made with nickel nitrate precursor at 4000 rpm. | 46 |
| Figure 20 | J-V curve of PCBM vs. PTEG-1. | 48 |
| Figure 21 | Histograms of J-V characteristics of PCBM and PTEG-1 devices. | 49 |
| Figure 22 | Light soaking phenomenon in the champion cell. | 50 |
| Figure 23 | Absolute PCE (%) difference due to light soak- ing and EQE measurement of PTEG-1 cham- pion cell. | 51 |
| Figure 24 | Difference in performance 11mg/ml and 10mg/ml in PTEG-1. | 53 |

LIST OF TABLES

| | | |
|---------|---|----|
| Table 1 | Spincoating parameters including filter mesh. | 28 |
| Table 2 | NiO annealing program. | 29 |
| Table 3 | NiO thicknesses. | 44 |
| Table 4 | Device characteristics of PCBM and PTEG-1. . . | 48 |
| Table 5 | Light soaking of champion cell. | 51 |
| Table 6 | Spincoating recipes for two step anti-solvent treatment. | 55 |
| Table 7 | Devices made with anti-solvent treatment. . . | 56 |

Part I

BACKGROUND INFORMATION

The first part of the thesis includes the background information needed for understanding the results. In [Chapter 1](#) an introduction to the topic is given. [Chapter 2](#) will describe the theory of the physical processes inside the perovskite solar cell, and subsequently the material properties are described in [Chapter 3](#).

INTRODUCTION

Energy consumption worldwide has more than doubled in the last 50 years, and is continuing to rise.[1] The majority of this energy is produced by burning fossil fuel sources such as oil, coal, and gas. This has led to anthropogenic CO₂ emissions into the atmosphere, which is the predominant factor in the global warming of the earth.[2] The increase of the global temperature can lead to catastrophic effects concerning the environment and earth's climate. To fulfill the energy needs and simultaneously reduce the CO₂ emissions, there is the need for alternative sources of renewable energy. Photovoltaic devices are one of the options that show great promise in achieving this. The technology is based on the absorption of photons from the sun to excite electrons to a higher energetic state in semiconducting materials. By separating the electron and the resulting hole, an electrical current can be extracted from the device. During this process no greenhouse gases are emitted; thus, the energy production is fully renewable.

The oldest and commercially most successful photovoltaic devices are silicon-based. Although efficiencies of up to 24% for whole Si solar modules have been achieved [3], these panels are still thick and difficult to produce. An alternative to the Si solar cells are the thin film perovskite solar cells, which have reached efficiencies exceeding 21% till date.[4] Perovskite have shown to be better absorbers of solar radiation than Si and many other materials, allowing for very thin and flexible films.[5] Since less material is required the production costs would be lower. Furthermore, perovskite solar absorbers are solution processable, allowing for a large number of processing techniques such as spincoating, doctor blading, and dipcoating. Many of these techniques are relatively simple and can be upscaled, which can reduce the manufacturing costs significantly.

The optoelectronic properties of perovskites make them excellent for the use in photovoltaic devices. For example, 1) the band gap of the material can be adjusted by changing its constituents [6], 2) the optical absorption coefficient is higher than many other absorbing materials, such as GaAs, CdTe, and crystalline and amorphous silicon. [5], 3) it has high charge carrier mobilities and lifetimes [7], and hence good charge transporting properties.

In this thesis perovskite solar cells are investigated with an active layer of MAPbI₃ and a hole transporting layer (HTL) of NiO. The inorganic NiO was chosen since it is more stable (in air) than organic HTLs, and leads to a higher open circuit voltage (V_{oc} , which will be discussed in [Chapter 2](#)).[8] Two device structures were studied, where

the ETL was varied between PTEG-1 and PCBM. The solvent used to process this layer was varied between chlorobenzene and chloroform. The addition of the ternary solvent NMP to the perovskite solution combined with an anti-solvent treatment is also investigated in order to improve the fill factor of the devices.

THEORY

2.1 HYBRID INORGANIC-ORGANIC PEROVSKITES

Generally, perovskites are characterized by the chemical formula ABX_3 , where A and B are cations, and X is an anion. In the case of hybrid inorganic-organic, the A cation is an organic ion, for instance methylammonium or formamidinium, and the B cation is a divalent metallic ion, such as Pb^{2+} or Sn^{2+} . Finally the X is a halide ion, e.g. Br^- or I^- . The A and B cations have a 12-fold and 6-fold coordination respectively, where the B cation is surrounded by an octahedron of 6 anions as can be seen in [Figure 1](#). The highest symmetry possible for the perovskite structure is of the cubic form, but can be distorted to lower symmetry structures depending on the size of the ions.[9] Furthermore, the temperature can influence the phase, as seen in the commonly used methylammonium lead iodide ($MAPbI_3$) perovskite. This perovskite is tetragonal at room temperature, but becomes cubic at temperatures above 330 K, and orthorhombic below 160 K.[10] Hybrid inorganic-organic perovskites possess many beneficial properties for solar cells, such as high electron and hole mobilities up to $60 \text{ cm}^2\text{V}^{-1}\text{s}^{-1}$, and long carrier lifetimes of 100 ns, resulting in diffusion lengths up to 1 micrometer.[6] Furthermore the absorption coefficient is higher than many other photovoltaic materials, and the bandgap can be tuned anywhere from 1.5 to 2.3 eV.[6] All of these properties, including their use in photovoltaic operation, will be discussed in the following paragraphs. The material properties in the specific case of $MAPbI_3$ will be discussed in [Section 3.3](#).

2.2 PHOTOVOLTAIC OPERATION

When a photon is incident on the surface of a semiconductor it can be absorbed provided that the energy of the photon is equal to or larger than the bandgap of the semiconductor. The hybrid inorganic-organic perovskites described above are semiconductors with a bandgap between 1.5 and 2.3 eV. The moment a sufficiently energetic photon is absorbed, it excites an electron from the valence band to the conduction band. The electron and hole can be bound to each other by Coulombic forces. The neutral quasiparticle that emerges is called an exciton. In perovskites, however, this binding energy is low due to the high dielectric constant of the material. Since the binding energy is lower than the thermal energy (at room temperature), it allows for the separation of charge carriers, and therefore free movement

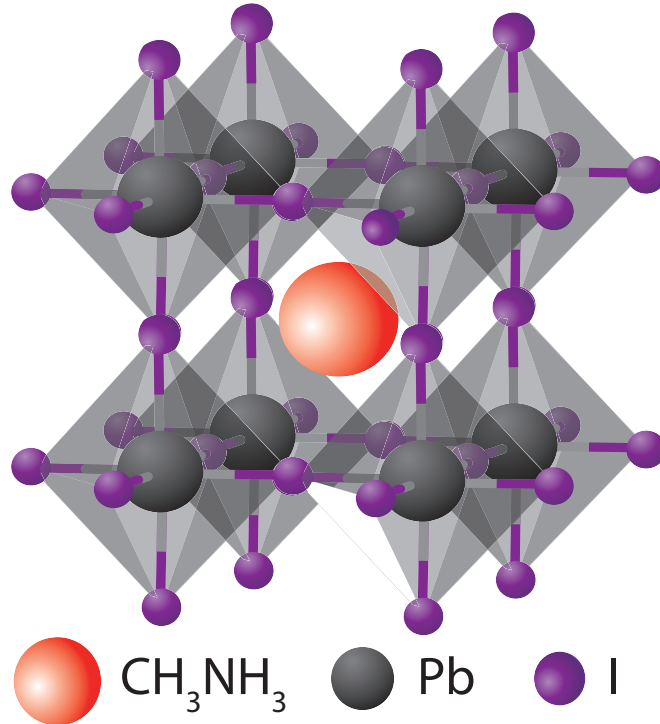


Figure 1: Hybrid inorganic-organic perovskite structure of MAPbI_3 . [Image made by Dr. Hong-Hua Fang (University of Groningen), used with permission.]

of these charges.[11, 12] In order to create a functioning solar cell, the photogenerated charges need to be extracted from the perovskite layer. Therefore, the perovskite layer needs to be connected to two electrodes, which allows the photogenerated electrons and holes to be extracted via the cathode and anode respectively.

2.2.1 Ohmic contact

When bringing two (semi)conductors into contact with each other, as is the case of perovskite and an electrode, the Fermi levels of both materials will align at thermal equilibrium, and the vacuum level will be continuous. As a result the energy levels will bend to fit these requirements, as can be seen in Figure 2 for a junction of a metal and an n-type semiconductor. If the work functions of the perovskite semiconductor and the metal electrodes lie far apart, large energy band bending will occur, introducing a Schottky barrier. If the Schottky barrier is sufficiently large, it will lead to the formation of a potential barrier for the charge carriers, preventing them from reaching the electrodes under equilibrium conditions.[13]

As seen in the energy band diagram of Figure 2, the Schottky barrier height ϕ_{Bn} for a junction of an n-type semiconductor and a metal

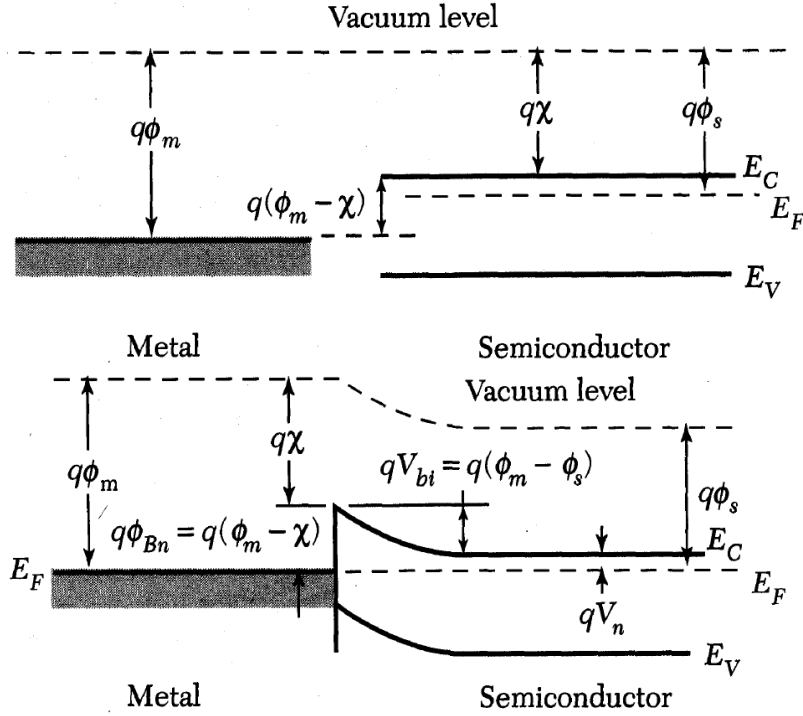


Figure 2: Energy band diagram of metal and an n-type semiconductor before (top) and after (bottom) contact. Here ϕ_m and ϕ_s are the work functions of the metal and semiconductor respectively, χ is the electron affinity of the semiconductor, and q the electrical charge. The energy levels of the conduction band, valence band, and Fermi level are given by E_C , E_V , and E_F respectively.[13]

depends on the electron affinity of the semiconductor and the work function of the metal

$$q\phi_{Bn} = q\phi_m - q\chi \quad (1)$$

Whereas for a p-type semiconductor it includes the bandgap energy E_g

$$q\phi_{Bp} = E_g - (q\phi_m - q\chi) \quad (2)$$

The term Schottky *barrier* might be confusing, since it implies an obstruction or blockade of some sort, however, a Schottky barrier does not necessarily block the relevant charge carriers. What matters is the built-in voltage (V_{bi}) that the charge carriers feel when trying to move from the semiconductor into the metal. The built-in voltage for an n-type semiconductor is given by

$$V_{bi} = (\phi_{Bn} - V_n) = (\phi_m - \chi) - (\phi_s - \chi) = (\phi_m - \phi_s) \quad (3)$$

where qV_n is the energy difference between the Fermi level and the conduction band of the n-type semiconductor. If the built-in voltage is positive ($V_{bi} > 0$), the electrons moving from the n-type semiconductor into the metal will feel a potential barrier, and will not be able to reach the metal without help of an external bias. Likewise, if the built-in voltage is negative ($V_{bi} < 0$), the electrons are not blocked, and able to freely flow into the cathode. The same holds for a p-type semiconductor, however, V_{bi} is defined differently as

$$V_{bi} = (\phi_{Bp} - V_p) = (E_g - (\phi_m - \chi)) - (E_g - (\phi_m - \chi)) = (\phi_s - \phi_m) \quad (4)$$

Therefore, in order to get ohmic contact, $\phi_s > \phi_m$ for an n-type semiconductor, and $\phi_s < \phi_m$ for a p-type semiconductor.

To summarize: the criterion that determines whether an electrode allows charge carriers to freely enter from a semiconductor, is the built-in voltage V_{bi} . As can be seen from [Equation 3](#) and [Equation 4](#), the built-in potential only depends on the work functions of the metal and the semiconductor. To create an ohmic contact thus requires careful selection of materials with matching energy levels. Disclaimer: this holds for Schottky devices, and doesn't take into account surface states of a semiconductor that might lie in the forbidden band gap. These states can cause effects called Fermi level pinning, which will not be discussed in this thesis.

2.2.2 Charge separation

As mentioned previously, a prerequisite for a functional solar is the selective charge extraction. Electrons need to be extracted at the cathode, and holes at the anode. To facilitate this, both charge separation and ohmic contacts are required. For this purpose an n- and p-type semiconductor layer are inserted at the cathode- and anode-interface, respectively, with the perovskite in between. In n-type semiconductors the majority charge carrier is the electron, indicating that the electron concentration is larger than the hole concentration. In a p-type this is exactly the opposite. Immediately upon connection of (one of) the semiconductors with the perovskite, the majority carriers will diffuse into the perovskite, and opposite charge will diffuse into the charge transport layer. This interface resembles a p-n junction, shown in [Figure 3](#).

Since the diffusing charge carriers from the two semiconductors are of opposite charge, they will recombine resulting in a depletion region, which is devoid of any free charge carriers. A net charge arises from the remaining ionic charges in the depletion region, that subsequently creates a potential difference, and therefore, an internal electric field ϵ_0 across the depletion region. This causes a drift of charge carriers in the opposite direction of the diffusing carriers. The drift

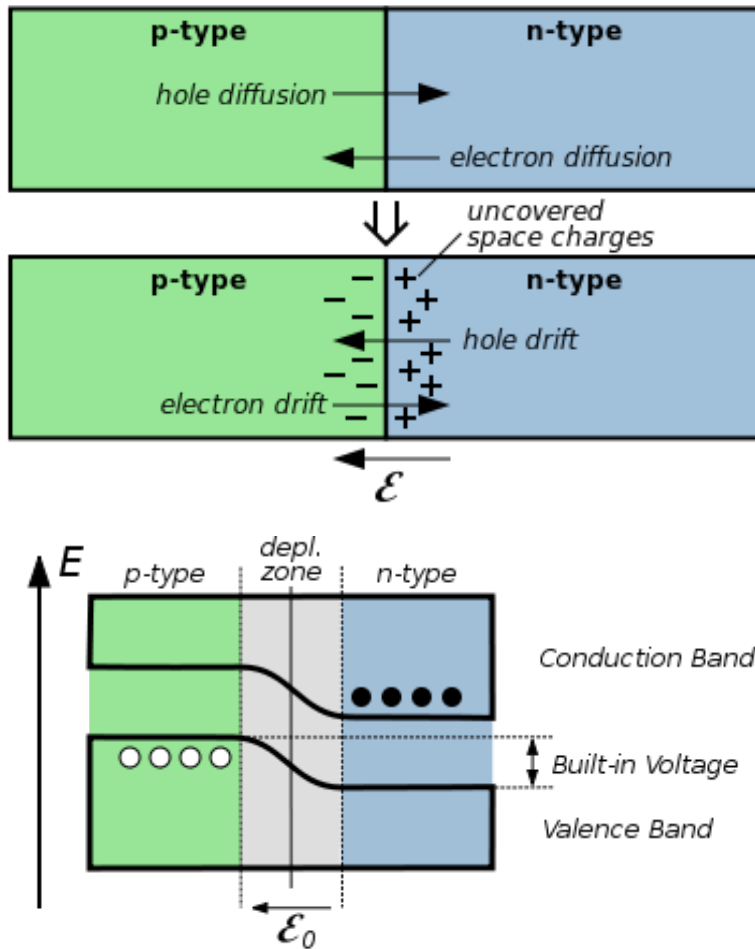


Figure 3: Charge diffusion and drift at interface of p- and n-type semiconductor (top), energy band diagram of same setup (bottom) in equilibrium.[14]

counteracts the diffusion of charge carriers and leads to an equilibrium between both. As a result, there will be no net current in the steady-state situation.

To create a net current, the built-in voltage barrier must be overcome. This can be achieved by applying a positive voltage to the p-side with respect to the n-side, also known as a forward bias voltage. The potential barrier is reduced to $V_{bi} - V_{external}$, which is equivalent to an electric field ϵ_{ext} working against the internal electric field, reducing the depletion region in size (Figure 4). Reversing the applied voltages to a reverse bias produces a larger potential barrier, since the applied voltage is now negative. This results in a larger electric field, and hence larger depletion region. The increased potential difference will make it increasingly difficult for the majority carriers to cross the depletion region. This means the charges in the device will only create a net current when a forward voltage is applied, therefore acting as a diode.

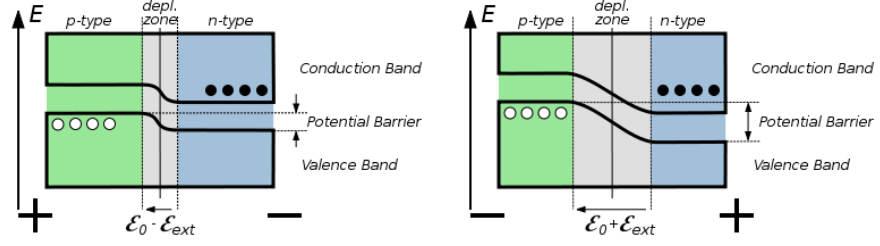


Figure 4: Externally applied forward (left) and reverse (right) bias on a p-n junction.[14]

2.3 SOLAR CELL CHARACTERIZATION

The p-n junctions present in the solar cells cause the device to behave as a diode, and its current-voltage characteristics can therefore be described by the Shockley diode equation under illumination

$$I = I_0 \cdot \left(e^{\frac{V}{n \cdot V_t}} - 1 \right) - I_L \quad (5)$$

with I_0 the reverse saturation current, also known as the dark saturation current. This current is measured at reverse bias in the dark, and is caused by thermal activity. Furthermore, V is the voltage across the diode, n the ideality factor, I_L the photogenerated current, and V_t the thermal voltage given by

$$V_t = \frac{k_B \cdot T}{q} \quad (6)$$

with k_B the Boltzmann constant, q the elementary charge, and T the temperature in kelvin. The thermal voltage is in the range of 25 mV at room temperature. A plot of the Shockley equation for an ordinary solar cell diode is given in [Figure 5](#).

As can be seen, the entire curve shifts down by I_L when the solar cell is illuminated. This current originates from the creation of electron-hole pairs in the photoactive perovskite layer after absorption of photons. The electrons need to diffuse to the interface with the n-type semiconductor, where they will drift through the depletion zone due to the electrical field. Similarly, the holes need to diffuse to the interface with the p-type semiconductor, followed by drifting through the depletion zone. In case the whole perovskite layer is depleted, no diffusion is necessary and drift takes over. Once the charge carriers reach their respective charge transport layer, the carriers become majority carriers and will not recombine with their counterpart. The carriers are now able to flow into the electrodes and create a net current. Inside the perovskite, however, recombination of free electrons and holes can still occur. The average length that the charge carriers can diffuse before recombining is called the diffusion length;

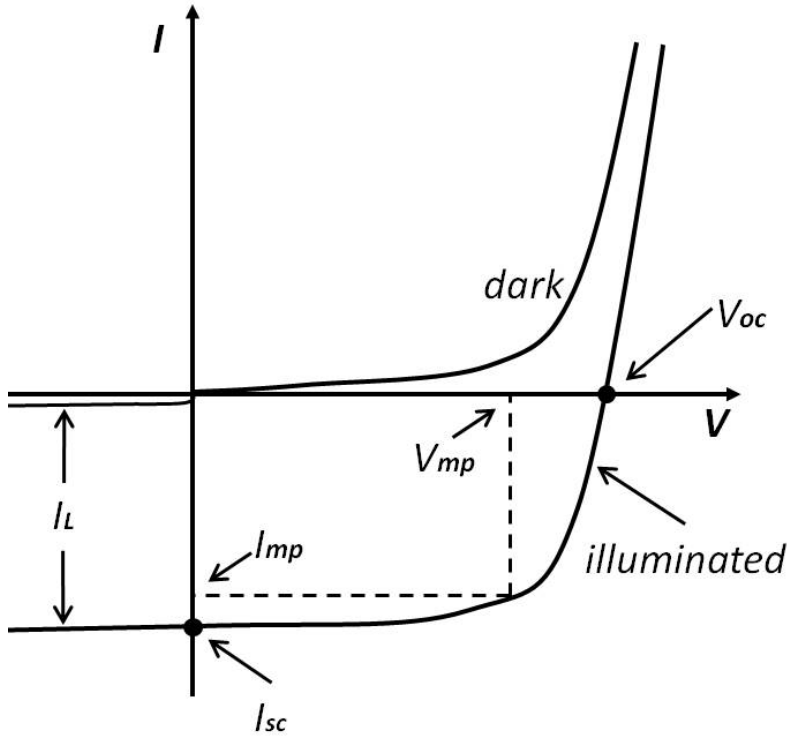


Figure 5: Current-voltage curve of a (non-ideal) solar cell diode in dark and under illumination.[15]

the time during which the carrier can diffuse before recombining is called the lifetime. Since the current flows against the applied bias, the illuminated graph is shifted downwards, and as a consequence, power can be extracted from the device. What can furthermore be determined from the curve are the open-circuit voltage (V_{oc}) and the short-circuit current (I_{sc}), which are respectively the maximum voltage and current that can be generated in the solar cell. However, no power can be extracted at these values, since $P = I \cdot V = 0$. For this reason the expressions I_{mp} and V_{mp} are defined, which are the current and voltage values at which the maximum power can be extracted. Subsequently, the power conversion efficiency (PCE) of the solar cell can be determined when illuminated by a power density P_{in} by

$$PCE = \frac{I_{MPP} \cdot V_{MPP}}{P_{in}} = \frac{I_{sc} \cdot V_{oc} \cdot FF}{P_{in}} \quad (7)$$

where the fill factor (FF) is defined as the ratio of the maximum obtainable power to the product of I_{sc} and V_{oc} , or in mathematical sense $FF = (I_{mp} \cdot V_{mp}) / (I_{sc} \cdot V_{oc})$. The fill factor is a measure of the shape of the I-V curve. A high fill factor corresponds to a sharp curve, and therefore a relatively large maximum power point and efficiency. The fill factor is reduced by components in the device exhibiting parasitic behavior. The non-ideal device can generally be described as an

ideal solar cell with two additional resistances, as is represented by an equivalent circuit diagram shown in [Figure 6](#).

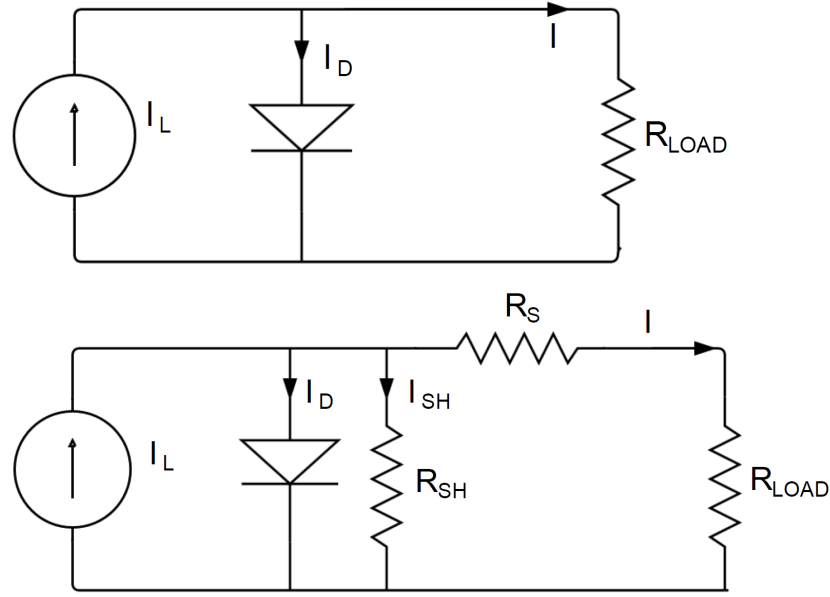


Figure 6: Equivalent circuits of an ideal (top) and non-ideal solar cell (bottom).[16]

One resistor is in series and accordingly called the series resistance R_s , and the other is the shunt resistance R_{sh} , which is in parallel with the diode. The series resistance mainly arises from the contact resistance of the interfaces of the different materials, and the resistivity of the materials themselves, e.g. in the metal contacts and the poorer conducting charge transport layers. The shunt resistance is due to defects in the device, opening up an alternate path for the current to leak through. If the shunt resistance is low, charges can easily flow through this alternative path, increasing the leakage current. The influence of these resistances on the fill factor is depicted graphically in [Figure 7](#). To increase the efficiency of the solar cell it is therefore essential to achieve a high shunt resistance, while keeping the series resistance at a minimum. The I-V curve including the resistors can mathematically be described by [Equation 8](#).

$$I = I_0 \cdot \left(e^{\frac{V+IR_s}{n \cdot V_t}} - 1 \right) - I_L + \left(\frac{V + IR_s}{R_{sh}} \right) \quad (8)$$

2.4 ENERGY LOSS MECHANISMS

2.4.1 Recombination

As briefly mentioned in [Section 2.2](#), when a solar cell absorbs a photon and the photogenerated holes and electrons are not extracted by

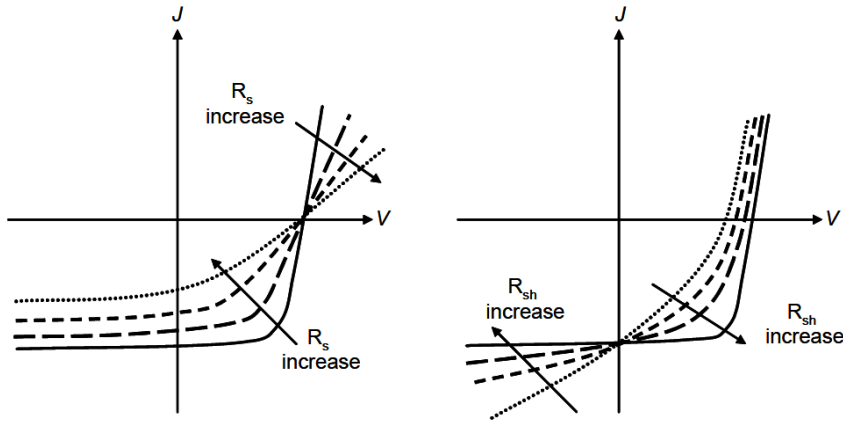


Figure 7: Influence of R_s (left) and R_{sh} (right) on the shape of the J-V curve.[17]

their respective transporting layers in time, the excited electron will stabilize back to the valence band and recombine. The photon energy that was originally absorbed will be re-emitted by the electron as a photon, and as a result, cannot be harvested. This is known as radiative recombination. The lifetime of the meta-stable excited electron state depends on the material, but can be up to 100 ns in perovskites.[7]

In the ideal case, a perovskite solar cell would be free of defects. In practice, however, this is hardly achievable. The defects that are present can cause the so-called Shockley-Read-Hall recombination to occur. This happens when a defect creates an energy state in the forbidden bandgap energy range of the perovskite. An excited electron or hole can subsequently be trapped by this energy state, which means it will be unable to be extracted to the transporting layer. As a result, the charge carrier will recombine. Since the charge carrier is “trapped” in the energy state, this process is also called trap-assisted recombination. During the relaxation of the electron to the trap state and finally the valence band, it transfers this energy to the perovskite in the form of phonons.

2.4.2 Bandgap losses

In case the perovskite absorbs a very energetic photon, whose energy is larger than the bandgap of the semiconductor, an electron will be excited to a higher state in the conduction band. The electron will quickly relax to the bottom of the conduction band, and in doing so, will release energy as heat in the form of phonons. This energy can not be extracted and is therefore lost. Increasing the bandgap of the perovskite allows for the utilization of this extra energy, however, it also causes a reduction in total photons absorbed, since the minimum photon energy has increased and a smaller portion of the photons

emitted by the sun will have this increased energy. When considering the solar spectrum, there exists an optimal value for the bandgap at which the efficiency of the solar cell is at its maximum theoretical value. This limit is known as the Shockley Queisser limit, named after the two people who studied this limit back in 1961. The limit is roughly 33% efficiency in the case of a single semiconductor with a bandgap of 1.34 eV and is based on the Air Mass 1.5 Global (AM1.5G) solar spectrum, seen in Figure 8.[18] If the sun is at less of an angle than 90° with respect to the surface, it will travel through more atmosphere than just the thickness. AM1.5 means it travels through 1.5 times the thickness of the atmosphere, which corresponds to a solar angle of roughly 48° , and is commonly used as a yearly average for mid-latitude regions such as Europe.[19] The AM1.5D is the irradiance from direct sunlight, while AM1.5G includes diffused reflected light from the sky and ground integrated over the hemisphere.

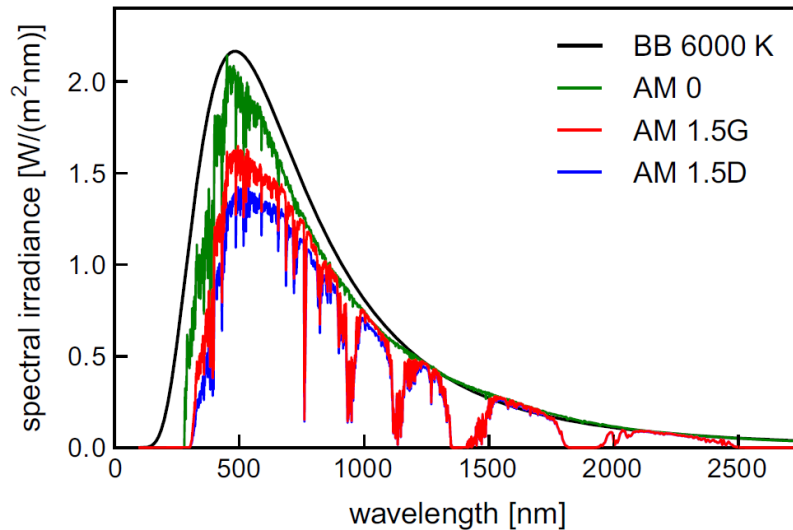


Figure 8: The solar spectrum in the case of 0 air mass, 1.5 air mass direct sunlight, and 1.5 air mass including reflected light integrated over the hemisphere, compared to a black body radiator with a temperature of 6000 K.

2.5 UNDESIRABLE BEHAVIOR

2.5.1 Hysteretic behavior

Hysteretic behavior in the current-voltage characteristics is currently one of the biggest challenges to resolve concerning perovskite solar cells. It is commonly seen that in reverse voltage scans the perovskite solar cells perform better than in forward scans, making it difficult to determine the actual PCE.[20–22] An example hereof is seen in Figure 9.

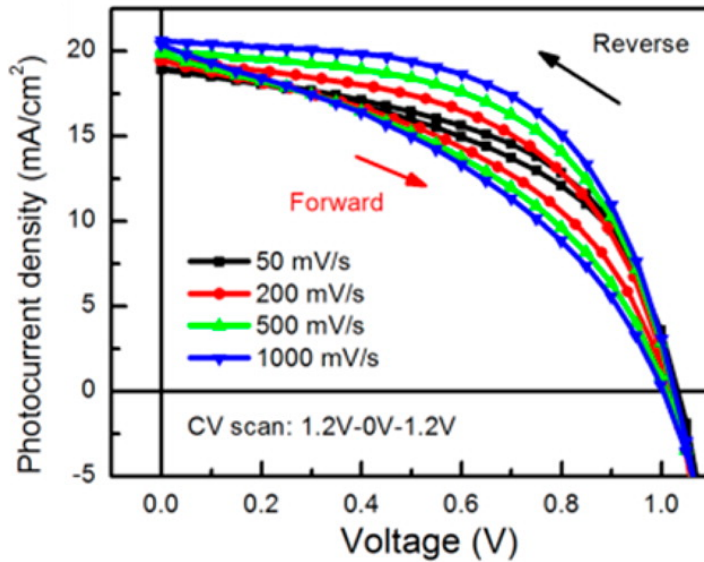


Figure 9: An example of a device with hysteretic behavior, where the magnitude of the hysteresis is influenced by the scanning rate.[21]

Parameters such as the voltage scan rate, direction, and range can influence the hysteresis.[21] Increasing the scanning rate, for example, can possibly increase the FF of the reverse scan, while decreasing it in the forward direction. Although the origin of the hysteresis is still under debate, several mechanisms have been proposed to explain the behavior:

Charge trap states due to defects

Trap states at the interfaces of the materials can contribute to the hysteresis. In this case the trap states fill under forward scan, while being depleted under reverse bias. The trap states arise from defects close to or at the interfaces between the layers. Wojciechowski *et al.* performed experiments in which they modified a titanium oxide (TiO_2) ETL with a C_{60} self assembled monolayer, resulting in a passivation of the trap states near the interface, and therefore reducing the hysteresis.[23] It has been suggested that the trapping and releasing of the electrons at the trap states changes the band bending, and hence the extraction of charges. Since the trapping process is dependent on the bias applied, it would therefore explain the hysteresis seen.[21] Studies have shown, however, that the trapping happens in milliseconds, which makes it unlikely to be the sole cause of the hysteresis according to some, since the hysteresis behavior occurs at much larger time scales.[24, 25]

Ferroelectric polarization

MAPbI_3 and similar hybrid perovskites have shown ferroelectric properties and domains, which could cause a slow polarization of the layer

when placed under bias.[22, 26] Polarization of the perovskite material can subsequently result in a change of charge extraction at the electrodes and hence hysteresis. Contradictions to this explanation for the hysteresis have arisen in a study by Beilsten-Edmands *et al.*, in which they conclude that the hysteresis behavior can not be assigned to the ferroelectric properties of the MAPbI₃, but is most likely due to ionic migration.[26]

Ionic migration

The idea of ionic migration, as was briefly mentioned in the previous paragraph, was proposed by Snaith *et al.*[22] back in 2014. It discussed that, under an applied bias, ions are able to move through the perovskite film and accumulate at the electrodes. The accumulated ions would in turn affect the band structure by locally changing the built-in electrical field. This influences the charge separation and extraction of the carriers. Since ion motion is much slower than the (de)trapping of electrons in trap states, it corresponds well with the time scale of the hysteresis. Especially the I⁻ ions in MAPbI₃ layers seem to be the cause for the hysteresis, as is discussed and modeled by Richardson *et al.* [20] The study also mentions that the trapping of electrons is not ruled out, and that it could very well be a combination of both these mechanisms that cause the hysteresis.

2.5.2 *Light soaking phenomenon*

When irradiating a perovskite solar cell continuously an interesting phenomenon can occur: the device performance increases, after it will reach a maximum, and after that possibly deteriorates. This unstable behavior is known as the light-soaking effect, and besides hysteresis, is one of the drawbacks perovskite solar cells still face. Several mechanisms have been suggested for the cause of the light soaking effect, which include the (de)filling of charge trap states under illumination [27] and the migration of ions to the electrodes [28]. Similarly to the case of hysteresis, the filling of trap states is debated intensively, since this mechanism does not seem to fit the long time scale of the light soaking. On the other hand, studies on ionic migration have shown more promising results. Cacovich *et al.* have used Scanning Transmission Electron Microscopy together with Energy Dispersive X-ray spectroscopy to determine the chemical changes of the MAPbI₃ perovskite that occur during light soaking.[29] Figure 10 shows their perovskite layer before and after light soaking. In this image it becomes apparent that the ratio of iodine to lead is reduced after light soaking, indicating that the iodine ions have migrated during this process. The iodine diffusion corresponds with the decrease of J_{sc} and rise of recombination processes in time.

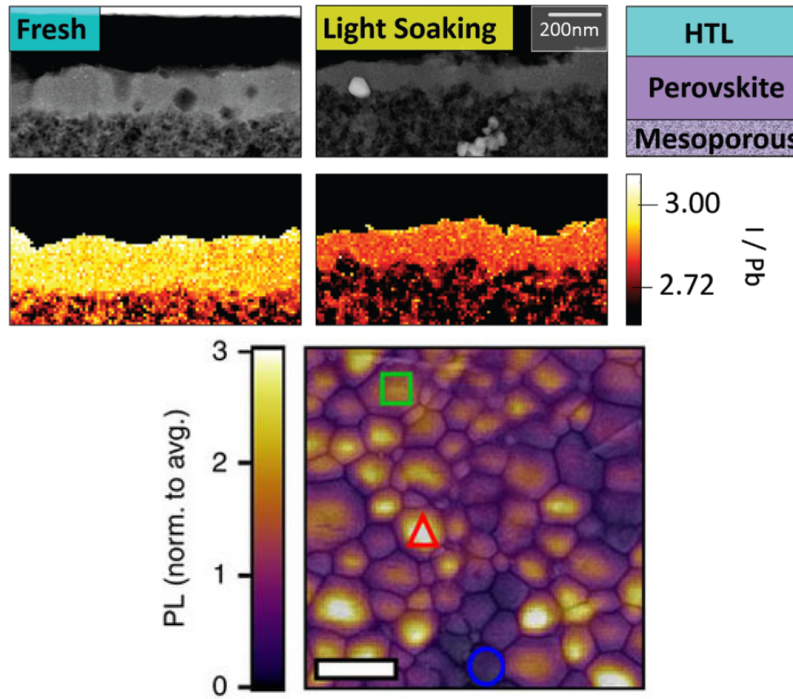


Figure 10: Iodine diffusion in MAPbI₃ layer (top)[29]; photoluminescence mapping of a thin MAPbI₃ film (bottom).[28]

Grain boundary influence

The photoluminescence of a thin MAPbI₃ film was measured by De-Quilettes *et al.*, as seen in Figure 10.[28] The grain boundaries are relatively dark, corresponding to a lower photoluminescence and therefore a higher trap state density at these locations. What was furthermore observed is the iodine migration away from the illuminated area, similar to Cacovich's study. Shao *et al.* have shown that the light soaking effect can be reduced significantly by creating compact perovskite films.[27] By making smaller and more compact perovskite grains, the grain boundaries are fused together, removing open grain boundaries. Since the open grain boundaries have a high density of trap states, the trap-assisted recombination is effectively reduced, which in their case also eliminated the light soaking phenomenon.

Difference in ETL

A different study by Shao *et al.* investigated the effect of a different ETL on the light soaking phenomenon.[12] Using the fullerene derivative PTEG-1 instead of PCBM as the ETL, they managed to eliminate most of the light soaking effect. The measurements indicate that the trap-assisted recombination at the perovskite-ETL interface is much larger in the case of PCBM than for PTEG-1, possibly explaining the reduction of the light soaking effect. Furthermore it is suggested that the side chains of the PTEG-1 could potentially passivate the trap states.

MATERIAL PROPERTIES

Various materials have been used for the fabrication of the perovskite solar cells in this thesis. Studying the materials of the various layers separately can give an insight in the working mechanisms of the device. For this reason this chapter is dedicated to describing the properties of each of the material used in this work.

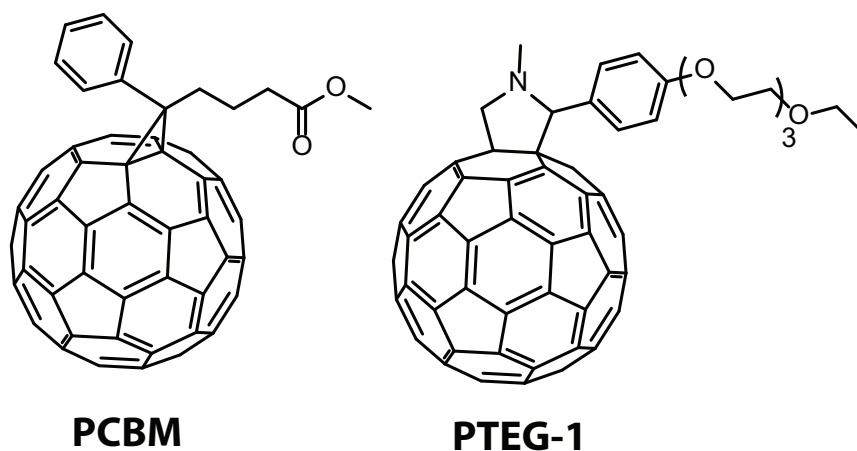


Figure 11: Structure of the fullerene derivatives PCBM and PTEG-1. [Image made by B.G.H.M. Groeneveld, MSc (University of Groningen), used with permission.]

3.1 ITO SUBSTRATES

The device substrate used for all solar cells consists out of a 3x3 cm thin piece of glass pre-patterned with indium tin oxide (ITO) contacts. Only cleaning of the substrates is required before device fabrication can start, as can be read in [Section 4.2](#). Glass is used because of its properties of being relatively flat, and transparent to the visible and a part of the infrared wavelengths. The configuration of the devices in this thesis is made such that light will be incident on the glass side. Transparency to light is therefore a prerequisite for the layers leading up to the perovskite. This is also the reason for choosing ITO, since in addition to being highly conductive, it is transparent. ITO is used in many optoelectronic applications because of its high work function of about -4.8 eV, making it a great material for an anode.[30]

3.2 NiO

The NiO layer functions as a transport layer for holes generated by the perovskite layer to the anode, hence this layer is called the hole transport layer (HTL). The work function of the NiO layer is roughly -5.4 eV [31]. This allows for charge transfer with the perovskite, and ohmic contact with the ITO layer, since the energy levels of these materials match each other. NiO has a large bandgap of over 3 eV (Figure 12), allowing the wavelengths of interest to pass through this layer to the perovskite without being absorbed. Besides being transparent, the large bandgap acts as a charge-selective barrier, blocking electrons from flowing to the anode. The benefits of using NiO instead of an organic HTL, are the higher stability (in air) and the fact that it leads to higher open-circuit voltages (V_{oc}) in solar cells.[8]

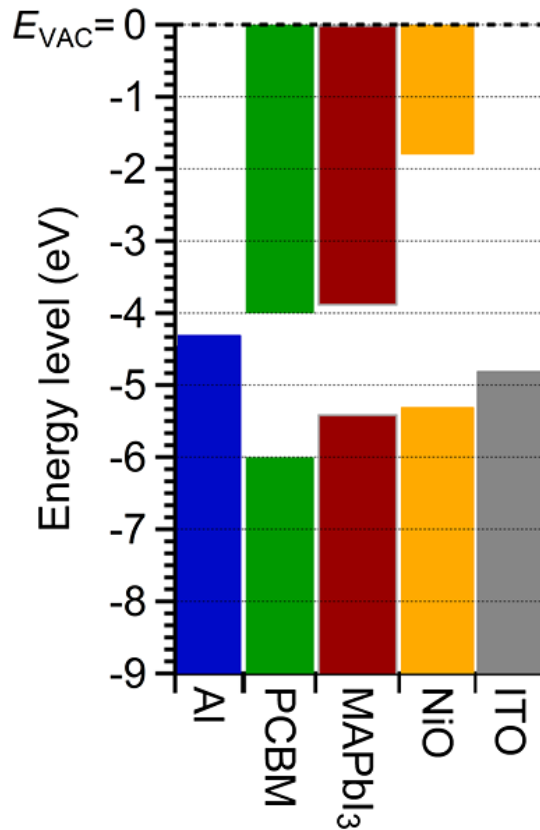


Figure 12: Energy band diagram of used materials.[7]

3.3 MAPbI₃

Methylammonium lead iodide (MAPbI₃) is currently one of the most commonly used active materials in perovskite solar cells. The bandgap of roughly 1.55 eV [7, 32] fits relatively well with the ideal Shock-

ley Queisser value of 1.34 eV, allowing for a potentially high PCE. The absorption coefficient of the perovskite is higher over a wide range of wavelengths than other frequently used photovoltaic materials such as GaAs, CdTe, crystalline and amorphous silicon, allowing for thin perovskite films of roughly 300 nm thickness.[5] The electron and hole diffusion lengths can range anywhere from 100 nm to > 1 micrometer, depending on the morphology and constituents of the MAPbI₃ layer.[33]

As was briefly mentioned in Section 2.2, the dielectric constant of MAPbI₃ has a value of (over) 6.5. As a result, the exciton-binding energies are estimated to be as low as 2 meV [34] to 10 meV.[11] These binding energies are smaller than the thermal energy at room temperature (25 meV), allowing for the separation of charge carriers, making the perovskite solar cells non-excitonic.

One of the major issues with MAPbI₃ is its stability under ambient atmospheric conditions. Aristidou *et al.* have studied the effect of oxygen on the degradation of MAPbI₃, and reported that simultaneous exposure to light and dry air resulted in the decomposition of the perovskite.[35] They suggest that the degradation is due to the electron transfer from the illuminated MAPbI₃ to the oxygen, creating a so-called superoxide. Subsequently the superoxide deprotonates the methylammonium, causing the decomposition of the perovskite into multiple components, including PbI₂. In contrary, Kim *et al.* showed that their perovskite solar cells remained stable over longer periods of time in dry air.[36] Since their solar cells were kept in the dark, it supports the findings of Aristidou *et al.* that both light and oxygen are needed for decomposition.

Water is another element present in ambient air which might cause degradation of the perovskite. This becomes evident from MAPbI₃ films which were kept in air with a relative humidity of 80% or higher. These perovskite films completely degraded within three days.[37] Studies done by Barnes *et al.* have demonstrated that the MAPbI₃ perovskite can be hydrated to a monohydrate structure, followed by further hydration to a dihydrate.[38] The latter transformation includes the dissociation of MAPbI₃ into PbI₂, and is suggested to be reversible. The addition of heat and/or an electric field can furthermore irreversibly decompose the monohydrate perovskite structure into PbI₂ and other constituents. [37] The fact that MAPbI₃ is soluble, makes it possible to solution process the layer with relative ease, as will be discussed in Section 4.1.

3.4 PC₆₀BM

PCBM ([6,6]-phenyl-C₆₁-butyric acid methyl ester), is a derivative of the C₆₀ Buckminsterfullerene molecule. It has a high electron mobility of $1 \cdot 10^{-2}$ to $2 \cdot 10^{-1}$ cm²/V [39], and high electron affinity with a con-

duction band level of about -3.8 eV (Figure 12).[40] This energy level is close to the conduction band of the perovskite, making it an excellent material for the electron transport layer (ETL) of the device. The organic solvents chlorobenzene or chloroform were used to dissolve PCBM in this thesis, allowing for spincoating of the layer, as described in Section 4.1.3. The bandgap of the material is 1.8-2.3 eV.[7, 40]

3.5 PTEG-1

An alternative material for the ETL is the slightly modified fullerene derivative called PTEG-1, which is a fulleropyrrolidine with a triethylene glycol monoethyl ether side chain. PTEG-1's and PCBM's structure are quite similar as illustrated in Figure 11; therefore, they have the same energy band levels. The solvents are identical as for PCBM. Shao *et al.* investigated the effect of PTEG-1 on the device performance when used as an ETL in a perovskite solar cell. They concluded that the PCE of the devices improved significantly, and the light soaking effect was reduced compared to PCBM.[12] The improvements seen in that study are the main reasons for trying out this material in this thesis.

3.6 ALUMINUM

Aluminum is used as the cathode, and has a work function of -4.3 eV [7], which matches well with the PCBM and PTEG-1 energy levels, allowing for ohmic contact. The layer does not need to be transparent, since it is used as the back electrode: light enters at the opposite side. The aluminum is deposited by means of thermal evaporation, which will be described in Section 4.4.

Part II

EXPERIMENTAL METHODS

Part two of the thesis focuses on the methods used in the experiments. The information concerning the device fabrication can be found in [Chapter 4](#), while the measurement techniques are discussed in [Chapter 5](#). A study is also done on the effect of different scrubbing methods on the surface morphology of ITO in [Chapter 6](#). Afterwards, in part three, the results of the experiments can be discussed.

DEVICE FABRICATION

This chapter describes the preparations and procedures regarding the device fabrication. A small change or error in one of the procedures can lead to poorly performing devices. For example, a dust particle of the size of 1 micrometer is already in the order of the device thickness. Such a particle would lead to shunts or shorts, and it is therefore that cleanliness is of great importance. For this reason the devices are prepared inside a cleanroom of class ISO 7.

The device substrates are cleaned thoroughly followed by spincoating of multiple thin layers, and finalized by thermal evaporation of the top contacts to create the structure of the device: ITO/NiO/MAPbI₃/PCBM or PTEG-1/Al. Background information for each material used in the device fabrication can be found in [Chapter 3](#). In order to make electrical contact with the solar cells, it is necessary for both the ITO and aluminum contacts to be exposed. It is therefore required to remove a small area of spincoated material covering the ITO before doing measurements.

4.1 SOLUTION PREPARATION

Depending on the materials and solvent, it can take anywhere between a couple of minutes to several hours to dissolve all the materials and create a proper solution. It is therefore that solutions are prepared one or more days in advance. Vials ranging from 4 ml to 20 ml are commonly used, and are made dust free by blowing in a stream of pressurized nitrogen. A magnetic stirrer is added to the vial to allow for automatic stirring on a magnetic (hot)plate. A scale with a resolution of 0.1 mg is used to weigh the materials. Micropipettes and syringes are used for solvent volumes up to 2 ml and larger than 2 ml, respectively. Prior to stirring the solution on the hotplate, the vial caps are sealed off with a plastic paraffin film (Parafilm) to prevent evaporation loss of the solvents.

4.1.1 *Nickel oxide precursor solution*

The nickel oxide precursor solution is made outside of the cleanroom in a fume hood. This is because the formation of the NiO layer requires elevated temperature in air, hence it is not possible to make the solution in the glovebox. The nickel(II) formate dihydrate (Alfa Aesar), is dissolved in ethylene glycol, creating a 0.5 molar solution. Next, 0.05 ml of ethylenediamine is added per ml of ethylene gly-

col. Both ethylene glycol and ethylenediamine were purchased from Sigma Aldrich. To make certain that the nickel salt is properly dissolved and has formed complexes with the ethylenediamine, the solution is stirred on a magnetic hotplate overnight at 50°C before use. The NiO is based on the recipe of Garcia *et al.* [41]

4.1.2 MAPbI₃ solution

The perovskite solution is prepared in a controlled atmosphere using anhydrous solvents, since oxygen and water deteriorate MAPbI₃ significantly.[37] For this reason a glovebox filled with nitrogen is used. In the glovebox water and oxygen molecules are kept below 0.1 parts per million (ppm) through the use of active circulation and filters. A 1:1 molar solution is made by mixing methylammonium iodide (MAI) with lead iodide (PbI₂) in solvents of γ -butyrolactone (GBL) and dimethylsulfoxide (DMSO) in a volume ratio of 7:3, based on the recipe by Jeon *et al.*[42]. Once mixed, the solution is stirred by means of the magnetic hotplate. The purities of MAI and PbI₂ are 98%, and 99.99% respectively, and were bought from TCI. The anhydrous solvents GBL and DMSO were purchased from Sigma Aldrich and Alfa Aesar respectively. In the experiment described in [Chapter 10](#) a ternary anhydrous solvent is added to the MAPbI₃ solution, namely N-methyl-2-pyrrolidone (NMP), which is bought from Sigma Aldrich.

4.1.3 PCBM and PTEG-1 solutions

Both PCBM and PTEG-1 solutions are deposited, and therefore also made, in the same glovebox as the perovskite. The glovebox protects the PCBM and PTEG-1 solutions from possible degradation due to environmental influences. The concentration of the PCBM solution is 20 mg/ml, while a concentration of 11 mg/ml is used for the PTEG-1 solution. The anhydrous solvents used for these solutions are either chlorobenzene or chloroform, purchased from Sigma Aldrich. PCBM was purchased from Solenne BV, while the fullerene derivative PTEG-1 was synthesized by the group of Hummelen from the University of Groningen. Similarly to the previous solutions, PCBM and PTEG-1 solutions are stirred on a magnetic hotplate before use.

4.2 SUBSTRATE PREPARATION

Prior to bringing the substrates into the cleanroom, they are dusted off by a pressurized nitrogen stream. The surface of the ITO layer contains a lot of peaks, and in case the peaks stick through the (multiple) fabricated layers, it will cause the device to short circuit, rendering the device useless. Smoothing out these peaks is achieved by scrubbing

the ITO contacts with scrubbing gloves for 5 minutes with lukewarm soapy water. This scrubbing will also help in removing any grease or dirt that might have been on the substrate. In [Chapter 6](#) the effect of scrubbing of the ITO surface is studied by AFM measurements, and its potential in reducing the number of shorts. After scrubbing, the substrates are placed into a beaker filled with type 1 deionized water, and the beaker subsequently placed into an ultrasonic bath for 5 minutes (power 5). When the 5 minutes are over, the sonication is repeated in a beaker with fresh, clean type 1 water. Next the substrates are moved to a different beaker and submerged in acetone, in order to dissolve and remove organic materials, and sonicated for 10 minutes (power 5). The final sonication step is in a beaker of isopropanol for 10 minutes (power 5), which due to its different polarity will dissolve other contaminants on the surface. To dry the substrates a pressurized stream of nitrogen is used to physically blow off a large part of the solvents, followed by 10 minutes in an oven at 120°C. Finally, the substrates undergo an O₂-plasma treatment for 2 minutes. This helps in removing any remaining organics and increases the wetting of the ITO and glass surface. In order to benefit from the increase in wetting, the O₂-plasma treatment is done just before spincoating of the first (NiO) layer. This, among other spincoating procedures, will be discussed in the following paragraph.

4.3 SPINCOATING AND ANNEALING PROCEDURES

One of the advantages of perovskite solar cells is that the active layer is soluble. This allows for solution processing, of which numerous techniques exist. The technique used in this thesis to create uniformly thin films is called spincoating. As the name suggests, spincoating involves spinning the substrate at high speeds. After dripping solution on the substrate, the spincoater accelerates to a previously set rounds per minute (rpm), resulting in a centrifugal force spreading the solution evenly over the substrate. The spinning velocity, acceleration and the time can be changed, allowing for control and optimization of the thin film.

The solution is filtered before deposition on the substrate to remove any unwanted aggregates, precipitants and impurities. The filter is connected to the output of the solution-filled syringe. The size of the filter mesh used for each spincoating procedure is given in [Table 1](#). When depositing the solution on the substrate, the wetting is of importance to the initial spreading of the solution. Depositing the solution and activating the spincoater should be done in rapid succession, especially in case the boiling point of the solvent is low (e.g. chloroform). If the process takes too long, the solvent starts to evaporate before spincoating is initiated, which results in a non-uniform layer. Ordinarily the spincoater is accelerated to the desired speed in

| Material | v (rpm) | a (rpm/s) | t (s) | lid | filter (μm) |
|--------------------|-----------|-------------|---------|--------|--------------------------|
| NiO | 4000 | 1000 | 80 | open | 0.45 |
| MAPbI ₃ | 1000 | 1000 | 40 | closed | 0.2 |
| PCBM | 1000 | 1000 | 60 | closed | 0.2 |
| PTEG-1 | 1000 | 1000 | 60 | closed | 0.2 |

Table 1: Spincoating parameters of the materials used, including the filter mesh size. The symbols v , a , and t stand for velocity, acceleration and time respectively.

a couple of seconds, at which it will remain for the set amount of time. The spinning velocity, the acceleration and the viscosity of the fluid determines the final film thickness of the film. Increasing the spinning velocity, or decreasing the viscosity of the solution, will result in a thinner film. Since the viscosity depends on the solvent and the concentration, these parameters are taken into account when optimizing a spincoating procedure. Finally there is the option to have a lid close off the spinning substrate. Closing the lid leads to a local environment saturated with solvent vapor. This means that the solvents have difficulty evaporating, and the film will remain wet longer. All the solutions in this thesis are spincoated in a nitrogen-filled glovebox, except for the nickel oxide precursor.

4.3.1 NiO procedure

The spincoating parameters for NiO are given in [Table 1](#). The entire surface is covered with the solution before activating the spincoater. After spincoating the nickel oxide precursor solution, the samples are moved in a Petri dish to a furnace, where the layer is annealed at 300°C for 1 hour in air to form NiO. See [Table 2](#) for the full oven program. The ethylenediamine that was added to the solution forms complexes with the nickel ions, allowing the formation of NiO at relatively low temperatures. The temperature of 300°C was chosen due to the good performance of the NiO layer, according to a study by Garcia *et al.* [41]

The resulting NiO layer is very hard, which is an unwanted side effect as it makes it difficult to remove the NiO covering the ITO contacts. To solve this problem, the samples are dried in an oven for 1 minute at 120°C immediately after spincoating. This results in a slightly solidified film, but still soft enough to allow for removing of the nickel with a scalpel. Ordinarily the NiO samples are left in the furnace overnight, and are taken to the cleanroom the next morning. The NiO samples are subsequently dusted off by a pressurized nitrogen stream before being moved into a steel canister. The canister

| Starting Temp. (°C) | Ending Temp. (°C) | Time (minutes) |
|---------------------|-------------------|----------------|
| N/A | 80 | 30 |
| 80 | N/A | 30 |
| 80 | 300 | 30 |
| 300 | N/A | 60 |
| 300 | 20 | 300 |

Table 2: Full NiO annealing program.

is sealed by an O-ring and is subsequently moved into the glovebox, where the remaining layers of the device are spincoated.

4.3.2 MAPbI_3 procedure

Five drops of the solution are applied on the middle of the device, before spincoating is initiated. As mentioned briefly in [Section 4.1.2](#), a similar recipe to Jeon *et al.*'s study was used. A difference in the MAPbI_3 procedure is the fact that they make use of an anti-solvent treatment, which is not the case in most of this thesis. In [Chapter 10](#) an experiment with anti-solvent treatment is used, but with specifications from a different study.[\[43\]](#) In this experiment the anti-solvent chlorobenzene is applied during spincoating of the perovskite layer. Chlorobenzene doesn't dissolve the perovskite, but does wash away the solvents used for the perovskite. This causes the crystallization of the perovskite during the spincoating, and results in a smooth film.

In order for the perovskite structure to form, the spincoated film has to be annealed. In the case of MAPbI_3 , the samples are placed on a hotplate kept at 100°C for 3.5 minutes. Higher temperatures could result in quicker evaporation, but on the other hand will also damage the MAPbI_3 layer, since thermal degradation will be accelerated.[\[44\]](#) The spincoating parameters of the MAPbI_3 layer can be found in [Table 1](#).

4.3.3 PCBM and PTEG-1 procedure

In this thesis PCBM and PTEG-1 are either dissolved in chlorobenzene or chloroform. Chloroform has a low boiling point of 61°C , which means that most of the chloroform evaporates during spincoating with an open lid. For chlorobenzene the boiling point is higher, around 131°C , which might result in slightly wet film after spincoating. The spincoating parameters are given in [Table 1](#). To ensure that all the remaining solvents have evaporated, the samples are kept in

vacuum for 1.5 hours inside the evaporation setup, where the last layer of the device is deposited.

4.4 THERMAL EVAPORATION OF ALUMINUM TOP CONTACTS

After all spincoating is finished, the samples are moved in the steel canister to another glovebox where the final layer is deposited by means of thermal evaporation. All devices in this thesis have final layers made out of aluminum, functioning as the top contacts. By moving the samples inside the nitrogen filled canister, they do not get into contact with any air, and should not degrade.

The evaporation setup includes an electrically conductive boat and a construction in which the samples are suspended upside down above the boat. The aluminum is placed into this boat, and a current is provided to create Joule heating. The heat causes the aluminum to melt and subsequently evaporate. To assist the evaporation, a metal bell jar is placed over the setup and a high vacuum (10^{-7} to 10^{-8} mbar) is created inside. Now the evaporated aluminum particles do not collide with any gas molecules, since it is in high vacuum, and can move directly to the sample surface, where they will condense to form the aluminum layer. Masks are placed in front of every substrate, covering the surface except for areas perpendicular to the ITO areas, to fabricate devices with well-defined active areas. This configuration ensures the accessibility of the ITO, while covering every device area with aluminum electrodes.

Besides the previously mentioned parts, the evaporation setup also contains a detector for particle flow and a shutter. By tuning the current through the boat, the rate of evaporation can be controlled precisely to sub $\text{\AA}/\text{s}$ ranges. The evaporation rate is manually set to $0.1 \text{ \AA}/\text{s}$ before opening the shutter. This rate is kept constant until a thickness of 2 nm has been reached, followed by an increase to $0.2 \text{ \AA}/\text{s}$ to a thickness of 5 nm. The rates are subsequently increased to $0.5 \text{ \AA}/\text{s}$ to 10 nm, $\text{\AA}/\text{s}$ to 20 nm and 1 to 2 $\text{\AA}/\text{s}$ to the final thickness of 100 nm, at which the shutter automatically closes. The slow starting evaporation rate serves as a method to carefully establish an interface by slowly evaporating small amounts of Al. After the aluminum top contacts have been deposited on the samples, the devices are complete, and can be measured immediately.

MEASUREMENT TECHNIQUES

The solar cell's performance can be understood by measuring its current-voltage response and doing external quantum efficiency (EQE) measurements. In this thesis the current-voltage response was measured by far the most, with nearly 2400 out of the 2700 total measurements. From this chapter onward, these measurements will be denoted as J-V measurements. Using the current density (J) namely makes it easier to compare different sized active areas. Next, thickness determination by the Dektak, ellipsometer, and XRR-setup are described. Finally, optical and atomic force microscopy methods are explained, which allow for surface studies of the individual layers.

5.1 J-V MEASUREMENTS

After finishing the device fabrication, the devices are transferred to the solar simulator glovebox via the steel container. As the name might suggest, the solar simulator glovebox is the glovebox where the sun's light is simulated. The lamp is turned on at least 15 minutes before measuring, in order to warm it up to reach the correct spectrum.

The source used is a Osram HMI 1200W/DXS lamp with an intensity of 1 sun, i.e. 100 mW/cm². The spectrum of the lamp spectrum approximates the solar spectrum corrected for the absorption and scattering of the light in the atmosphere and the angle of the sun with respect to the solar cell, namely that of Air Mass 1.5 Global (AM1.5G). Although the lamps are fabricated with these specifications in mind, they most likely will not match the AM1.5G perfectly.

To correct for this, the intensity of the lamp can be calibrated such that it matches the sun, by use of a silicon reference cell. The silicon reference cell can subsequently determine the spectral mismatch factor given by

$$M = \frac{\int E_R(\lambda)S_R(\lambda)\delta\lambda}{\int E_S(\lambda)S_R(\lambda)\delta\lambda} \cdot \frac{\int E_S(\lambda)S_T(\lambda)\delta\lambda}{\int E_R(\lambda)S_T(\lambda)\delta\lambda} \quad (9)$$

where E_R and E_S are the AM1.5G reference- and solar simulator spectra respectively. S_R is the spectral response of the silicon reference cell, and S_T is the spectral response of the tested solar cell. The responses of both the cells are determined by external quantum efficiency (EQE) experiments, explained in the following chapter. Dividing the measured current of the reference cell by the mismatch factor results in a corrected current. The height difference between the lamp and the

device has to be adjusted in order to calibrate the setup, since the lamp itself can not be altered. It is therefore that the silicon reference cell is shifted in height until it matches the corrected current value. At this height the intensity of the spectrum is calibrated to the solar spectrum, and consequently the devices can be measured.

All electrodes need to be accessible in order to make electrical contact with the device. Since the MAPbI₃ and ETL are still covering the ITO, a part of these layers is removed with a scalpel. Next, the devices are placed in a sample holder with eight pins used for making electrical contact, two per device area: one for the anode and cathode. A Keithley 2400 Sourcemeter is connected to the electrical contacts, which can measure the current response of the solar cell by applying a DC voltage. The voltage is swept in steps of 0.04 V from 0 V to 1.4 V, followed by going down to -0.4 V and back up again to 0 V, yielding a forward and backwards scan and revealing any hysteresis present. The data acquired from the measurements is analyzed by a software program called LabView on a computer connected to the Keithley. This software also allows adjusting of the voltage steps and ranges of the measurement. All device areas are measured individually in both dark and under illumination, and are kept at 295 ± 0.5 K by manually controlling a flow of cooled nitrogen. The area on the device where both the electrodes overlap is the area that is measured by the Keithley. To ensure that the measured current is not from surrounding regions, a mask with smaller openings is used during measurements under illumination.

5.2 EQE MEASUREMENTS

J-V measurements give an understanding on how the device acts under full light illumination while being biased. The external quantum efficiency (EQE) is the ratio of the number of extracted electrons to the number of incident photons on the solar cell. In order to determine the EQE, the spectral response S_T needs to be known, which is quantified by illuminating the device with monochromatic light with known power over a range of wavelengths. The EQE is consequently calculated by Equation 10, where h is Planck's constant, c the speed of light, q the elementary charge and λ the wavelength of the light.

$$\text{EQE}(\lambda) = \frac{hc}{q\lambda} \cdot \frac{J(\lambda)}{P_{\text{in}}(\lambda)} \quad (10)$$

To measure the EQE, the devices from the glovebox are placed into a holder similar to the JV-setup: eight pins for electrical contacts at the back, and a mask at the front. The difference, however, is the fact that the holder is sealed off by a glass window and is portable. This is necessary since the EQE setup is located in air, outside of the glovebox and cleanroom. The lamp used is a OSRAM 64655 HLX (250

Watt) lamp, whose light shines through an arrangement of three filter wheels. The wheels themselves contain multiple filters that, when combined, allow for 33 monochromatic wavelengths ranging from 380 to 1400 nm to be formed. The perovskite layer does not absorb over this entire wavelength range, and therefore only the range 380 to 800 nm is used during measurements. The power of the monochromatic light is measured by a photodetector (Ophir PD300 series) at a certain distance and height from the lamp. After all wavelengths have been measured, the photodetector is replaced by the device holder containing the solar cell, and the area that is to be measured is placed at the same height and distance from the lamp. The device holder is connected via a Keithley 2410 SourceMeter to a computer where Lab-View software is active. The software corrects for the size of the area that is measured and the Keithley measures the current produced by the solar cell.

5.3 THICKNESS MEASUREMENTS

Multiple measurement setups for determining the thickness of the solar cell layers were used in this thesis. Two of which use photons, i.e. an ellipsometer and a setup for X-Ray Reflectivity (XRR), and one that mechanically profiles the surface: the Dektak.

5.3.1 *Dektak*

The Veeco Dektak 6m Profilometer is kept in the cleanroom, outside of the glovebox. It creates a profile by scanning over the surface of the sample with a tip, which gives an indication of the height distribution of the sample. To measure the thickness of one or multiple layers, a scratch has to be made that goes down to the glass substrate. A step in the profile is now noticeable when scanning perpendicularly across the scratch. By measuring the height difference of the step, the thickness of the layers can be determined. The Dektak can profile height differences from a few nanometers up to several micrometers.

5.3.2 *XRR*

For X-Ray Reflectivity measurements, a PANalytical X'Pert diffractometer providing monochromatic Cu K- α x-rays was used. The energy of these x-rays is 8.04 keV, which corresponds to a wavelength of 1.5406 Å. A sufficient amount of x-rays need to be reflected from the sample into the detector in order to determine the thickness. This limits the maximum thickness of the films to roughly 100 nm and the surface roughness to about 5 nm.[45] During a measurement the angle theta of the x-rays with respect to the sample is varied slightly (0 to 8°) and the reflected rays are collected at the detector. The intensity

of the reflected rays will oscillate depending on the angle. These oscillations are called Kiessig fringes, and from the period the thickness of the layer can be determined by

$$\Delta Q = \frac{4\pi}{\lambda} \sin(\Delta\theta) = \frac{2\pi}{D} \quad (11)$$

where ΔQ is the difference in wavevector, $\Delta\theta$ the difference in angle of the period, λ the wavelength of the x-rays, and D the thickness of the layer.[46]

5.3.3 Ellipsometer

The thickness of a layer can be determined by shining linearly polarized light onto the sample and measuring the change of the polarization. A part of the transmitted light is reflected on the interface of the film and the underlying substrate and will rejoin the reflected light on the surface and interfere. Comparing the polarization of the incoming beam with the reflected beam and matching it with a model, multiple parameters, including the thickness, of the film can be extracted. Films with a thickness in the range of subnanometer to a few micrometers can be measured, unless it is strongly absorbing the incoming light.[47] The ellipsometer that was used is the VB-400 V-Vase Ellipsometer from J.A. Woollam Co., Inc. The scans were performed over the wavelength range of 400 to 1700 nm.

5.4 OPTICAL MICROSCOPE

The optical microscope uses visible light to image the surface of the sample. The light that is reflected from the sample is magnified by a system of optical elements, such as lenses. The optical microscope used in this thesis is the Olympus BX51M with lenses of 5x, 10x, 20x, 50x, and 100x magnification. The diffraction limit of optical microscopes with conventional lenses allows for a theoretical resolution up to roughly 200 nm.

5.5 AFM MEASUREMENTS

Atomic-force microscopy (AFM) is a measurement technique that can image the topography of the surface down to subnanometer resolution, which is far greater than the magnification possible by the optical microscopy diffraction limit. A cantilever with a small tip is moved close to the surface of the substrate. A laser shines at the backside of the cantilever, and is reflected into a photodetector. Once the tip is within close proximity of the surface, attractive and repulsive forces come into play. These forces will cause a displacement of the

cantilever, and thus the reflection of the laser will be displaced as well. A piezoelectric device allows for precise movement of the probe over surface. The topographic image is consequently created by measuring the displaced reflection of the laser and converting its signal. The Bruker MultiMode Atomic Force Microscope MMAFM-2, using ScanAsyst-air tips were specifically used in this thesis.

INFLUENCE OF ITO SCRUBBING METHOD

Manually scrubbing the ITO surface is tedious work. In order to improve this process, a study is done on the effect of different scrubbing methods on the surface morphology of the ITO substrate. It is assumed that the peaks of ITO on the glass substrate are large enough to stick through spincoated layers of e.g. NiO, which can result in unwanted alternative pathways for the charge carriers. By manually scrubbing the ITO contacts for 5 minutes with lukewarm soapy water, one can smoothen out these peaks considerably, reducing the amount of shunting pathways.

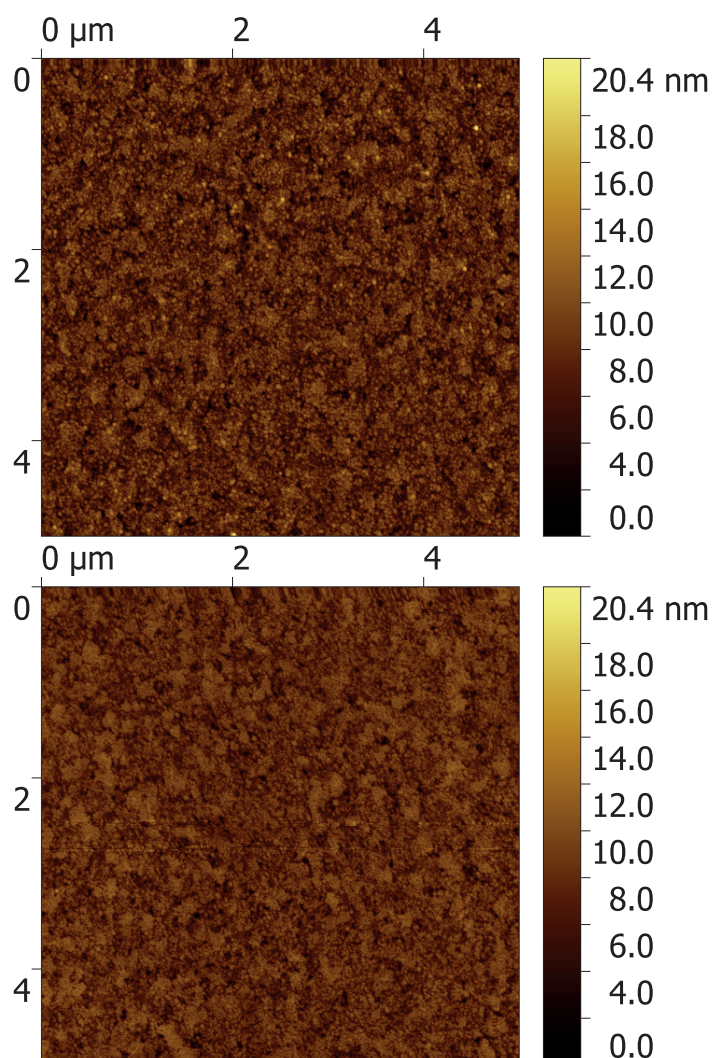


Figure 13: An ITO substrate before (top) scrubbing, and after (bottom) scrubbing by hand.

Using multiple scrubbing methods and subsequent examination of the morphology by using an AFM, will hopefully give useful information about the influence and necessity of the scrubbing. Eliminating the need for scrubbing could result in a reduction of preparation time of up to one hour per experiment.

6.1 DIFFERENT SCRUBBING METHODS

An AFM image of the morphology of the ITO contact before and after manual scrubbing are visible in Figure 13. Before the samples were put into the AFM, they were cleaned similarly to Section 4.2, except for the initial step, which included a 5 minute long ultra-sonication in soapy type 1 water. It is evident from Figure 13, that the scrubbing smoothens out the peaks. The height difference between the minimum and the maximum of the ITO is 20.4 nm before scrubbing, and 14.7 nm afterwards. This reduction is due to the smoothing of the highest peaks, reducing their height.

Other scrubbing methods were also studied, including steel wool, the (rough) backside of a sponge, and diamond lapping paper with a roughness of 0.5 and 1 micrometers. Figure 14 shows the effect of the combination of 1 and 0.5 micrometer diamond lapping paper on the morphology. In this case the morphology is altered completely. Quite a lot of force was applied in one scrubbing direction, which likely explains the trenches seen on the surface. An extra experiment was conducted in which it was made sure to reduce the force, and vary the scrubbing direction. This led to the morphology seen in Figure 15. Steel wool managed to remove several peaks, but also created a few scratches (Figure 15). No image is shown of the sponge scrubbing, since this method did not lead to an observable difference compared to the morphology before scrubbing.

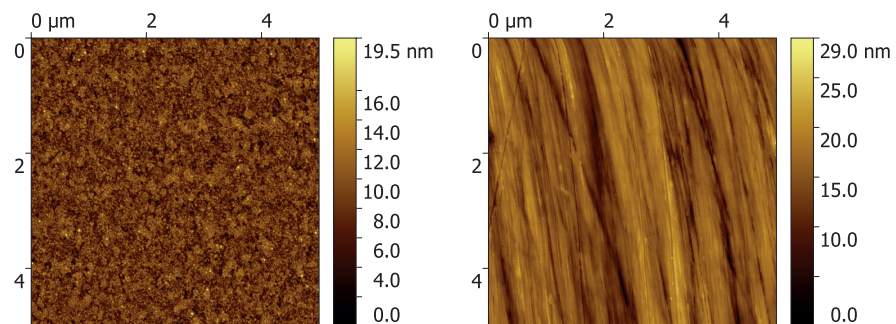


Figure 14: An ITO substrate before (left) scrubbing, and after (right) scrubbing with diamond lapping paper of 1 and 0.5 micrometer subsequently.

Without making large batches of devices it is difficult to say whether the new scrubbing methods lead to the same device performance as for manual scrubbing, since it depends on the thickness of the spin-

coated NiO layer. If the thickness of the NiO layer is measured from the lowest point on the ITO surface, then NiO layers thinner than 20 nm would seem unlikely, since it would result in ITO peaks sticking through this layer, resulting in poor performance of the device. Although the results from the previous chapter are not conclusive, most measurements point towards a NiO film (made from nickel formate) thinner than 20 nm.

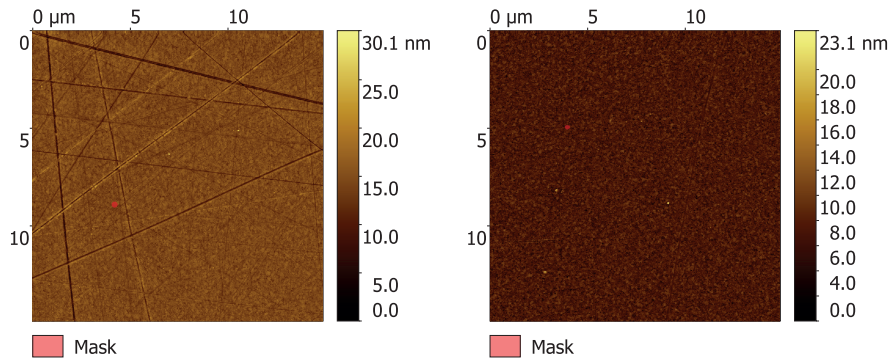


Figure 15: Scrubbed ITO substrates with diamond lapping paper of 0.5 micrometer (left) and steel wool (right). Parts of the images were masked in order to show the scratches that were made by the scrubbing methods.

Furthermore AFM measurements were done on fluorine-doped tin oxide (FTO), as seen in Figure 16. The height difference in this case is more than 200 nm. These substrates are used by group members in other solar cell devices.

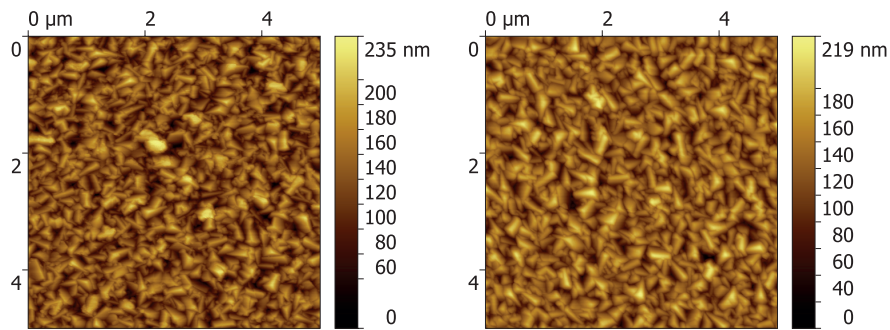


Figure 16: An FTO substrate before (left) scrubbing, and after (right) scrubbing by hand.

Ultimately it seems that the manual hand scrubbing method remains the best way to smoothen the ITO surface. It reduced the highest peaks on the measured substrate from roughly 20 to 15 nm. The newly introduced scrubbing methods resulted in either no change (sponge) or damage (diamond lapping paper & steel wool) to the surface morphology. Finally the FTO peaks were reduced slightly by scrubbing by hand, but remained in the order of 200 nm in height.

Part III

EXPERIMENTS, RESULTS AND DISCUSSION

The final chapters contain the experimental results including discussion. The experimental work mainly focuses on creating the device structure described in [Chapter 4](#), where the ETL layer and its solvent are varied. First of all, [Chapter 7](#) investigates the thickness and surface morphology of NiO layers made with different nickel precursors. Subsequently, in [Chapter 8](#), devices made with ETLs of PCBM and PTEG-1 are compared in performance. Next up devices containing ETLs made with chlorobenzene and chloroform are compared in [Chapter 9](#). Finally the addition of a ternary solvent to the MAPbI₃ solution and its influence on the PCE is studied in [Chapter 10](#). This experiment includes an anti-solvent treatment.

NICKEL OXIDE THIN FILM CHARACTERIZATION

A possibility of improving the perovskite solar cells is by enhancing the NiO hole transport layer. By doping the NiO layer with e.g. Cu, the hole conductivity of this layer can be improved, consequently increasing the FF and therefore the PCE.[48] Before doping is considered, the NiO layer itself should be optimized, and therefore multiple precursors should be explored. The NiO layers made with different precursors should have the same thickness in order to properly compare them in device performance. For this reason it was decided to initially start with thickness measurements before moving on to the device fabrication with these layers. Solutions with a concentration of 1 M of the precursors nickel(II) acetate tetrahydrate and nickel(II) nitrate hexahydrate were made, dissolved in 10 ml of ethylene glycol and 0.6678 ml of ethylenediamine, resulting in a 1:1 molar ratio of nickel salt to ethylenediamine. The nickel oxide precursor solutions were subsequently spincoated on glass substrates at 4000, 5000, 6000, and 7000 rpm for 80 seconds, with an acceleration of 1000 rpm/s in order to create NiO layers of varying thicknesses.

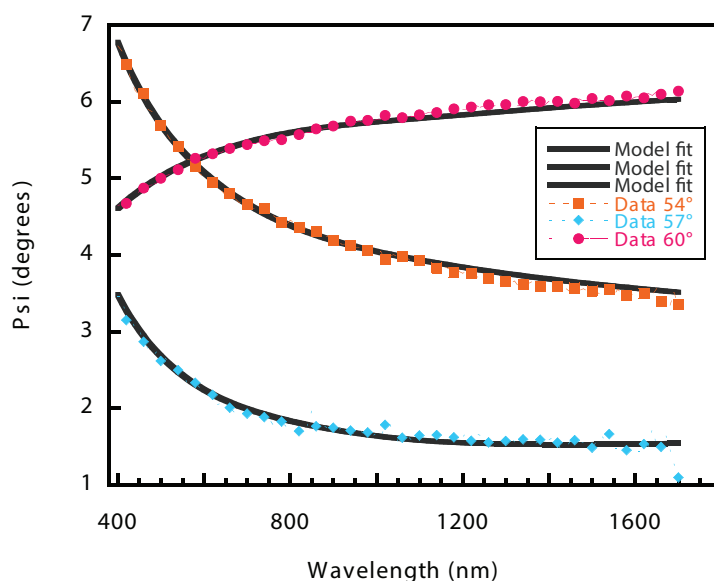


Figure 17: Nickel formate 0.5M solution prepared film at 4000 rpm on low iron glass (opaque backside). Thickness determination by ellipsometry.

| Ni precursor + substrate | XRR (nm) | Ellipsometry (nm) |
|-----------------------------|-------------|----------------------|
| Nitrate 1M soda lime | 41.4 | 76.4 |
| Formate 1M soda lime | 17.5 | N/A |
| Formate 0.5M soda lime | 7.5 | N/A |
| Formate 0.5M silicon wafer | N/A | 8.8 |
| Formate 0.5M Low iron glass | N/A | 19.4 |

Table 3: NiO thicknesses measured by XRR and ellipsometry of various substrates and precursors of different molarities. The thicknesses could not be measured by the ellipsometer on regular soda lime glass due to noise. XRR measurements on silicon and low iron glass were canceled due to time restrictions. All substrates were spincoated at 4000 rpm, according to the recipe in [Table 1](#).

7.1 THICKNESS MEASUREMENTS

Initially the Dektak was chosen to do thickness measurements, however, the profiler was unable to measure the thickness of the NiO accurately. The Dektak requires a step in the layer to be able to give an indication of its thickness. The step is commonly made by scratching the layer with a metallic tweezer or a scalpel. These tools are not able to penetrate the NiO layer, since it is too hard. A diamond pen was therefore utilized. The problem that arose with the diamond pen was the fact that it was scratching into the glass substrate, making the thickness measurements inconsistent. In order to create a step, two other methods were attempted. One method scratched the NiO layer before annealing, and the other method covered a piece of the substrate with tape before spincoating. Both methods failed. The scratch was partly filled back in during annealing, and the tape partly evaporated during annealing. This resulted in noisy and inaccurate Dektak measurements.

Two other measurement techniques were examined: x-ray reflectivity and ellipsometry. In the case of ellipsometry, a good contrast between the front and the back of the substrate in terms of opacity is required. Since the glass substrate is transparent on both sides, it was necessary to polish the backside of the substrate. This was done using rough sandpaper. The roughening did not always provide enough contrast, resulting in noisy measurements. To reduce the noise level, NiO was spincoated on Silicon wafers and on low iron glass substrates. The latter of which was opaque on the backside of the substrate. An example of a measurement, including fits for nickel formate is shown in [Figure 17](#). The thicknesses resulting from the fits are summarized in [Table 3](#).

As can be seen, not every measurement is present, due to time and/or noise restrictions. According to the XRR data the 0.5 M nickel(II) formate solution is roughly 8 nm thick. This is supported by the ellipsometer measurement on silicon, measuring about 9 nm. When the same solution is measured on low iron glass, however, the fit calculates a thickness that is more than double: 19 nm. Furthermore it seems to roughly double the size of the layer when doubling the concentration: the thickness increases from 7.5 to 17.5 nm, according to the XRR data.

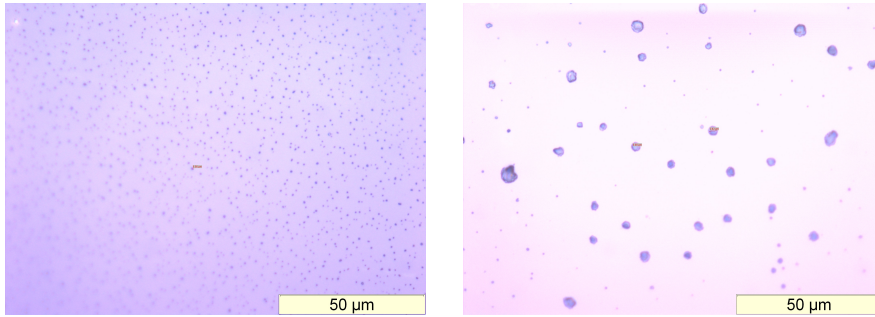


Figure 18: Optical microscope 50x zoom images of NiO thin film made with nickel nitrate precursor spincoated at 4000rpm.

7.2 MICROSCOPY MEASUREMENTS

Through the use of atomic force and optical microscopy, the surface morphology can be determined. Large particles in the size range of 0.3 to 5 micrometers are visible from the optical microscope in the case of NiO layers made with nickel nitrate, as seen in [Figure 18](#). These particles are a few hundred nanometers in height, according to AFM measurements ([Figure 19](#)), while the surface morphology excluding these particles is in the order of 20-30 nm in height. NiO layers made with the precursors of nickel formate and nickel acetate do not show these large particles, and instead are smooth. The reason for these particles might be due to the fact that the nickel salts have not dissolved properly, or have precipitated before spincoating.

Since a filter mesh with a size of 0.45 micrometers was used, it is most likely the latter.

To summarize: the NiO layer made with 0.5 M of nickel(II) formate seems to have a thickness of roughly 8 nm according to the XRR and ellipsometry data. Contrasting data is also seen from the ellipsometer measurement on low iron glass, giving a thickness that is more than double: 19 nm. Additional data from the XRR-setup shows that a doubling in the concentration from 0.5 M to 1 M seems to roughly double the thickness of the layer in the case of nickel(II) formate. No other conclusive arguments can be given, since data and statistics are lacking. It was therefore decided to focus on undoped NiO layers for

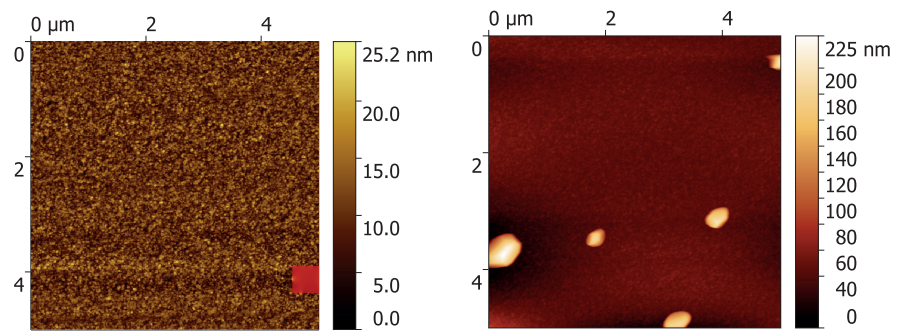


Figure 19: AFM measurements of NiO films made with nickel nitrate precursor at 4000 rpm. In the left image a particle is masked in red, which allows for the study of the rest of the surface.

use in the devices. The recipe for the NiO solution is described in [Section 4.3.1](#).

The solar cells that are discussed in this chapter were made according to the device fabrication as was explained in [Chapter 4](#). This leads to the structure of ITO/NiO/MAPbI₃/ETL/Al, where in this case the devices were made with ETLs of PCBM and PTEG-1.

8.1 LAYER THICKNESS

Thickness optimization of the MAPbI₃, PCBM, and PTEG-1 layers was done in previous work by Mehrdad Najafi. The spincoating parameters for these optimal conditions are discussed in [Chapter 4](#), and were used in the following experiments, unless stated otherwise. The thickness of the layers was determined by the Dektak to be about 50 nm for PTEG-1 and PCBM, and about 265 nm for MAPbI₃. Increasing the thickness of the PTEG-1 or PCBM results in an increased series resistance, and therefore lower FF and J_{sc} , while a decrease of the thickness can lead to less shunt resistance, decreasing the FF and V_{oc} , as can be seen in [Figure 7](#). An optimal thickness also exists for the perovskite layer. In this case the trade-off is between the absorption of photons and charge carrier diffusion length. A thicker layer will absorb more photons, and therefore create more charge carriers. However, if the layer is much thicker than the diffusion length of the created charge carriers, the carriers will recombine before reaching their respective transport layer.

8.2 DEVICE PERFORMANCE

In [Figure 20](#), the J-V curves of devices made with PTEG-1 and PCBM are compared. Two devices with an identical fill factor (in the reverse scan) were chosen, allowing for a proper comparison between the J_{sc} and V_{oc} of the devices. This choice can be justified by the fact that there seems to be no trend between the FF and the choice of ETL: in both cases the FF varies from low values (0.35) to high values (0.7), with no obvious champion, as can be seen in [Figure 21](#).

From the J-V curve ([Figure 20](#)) it is evident that the device made with PTEG-1 has a higher J_{sc} , and a slightly higher V_{oc} than PCBM. A strong hysteresis effect is also present in both devices. The values of the device characteristics for both forward and reverse scans are summarized in [Table 4](#).

It has been speculated that trap states at the interface of MAPbI₃ with the ETL/HTL are a cause of the hysteresis.[21] Passivating these

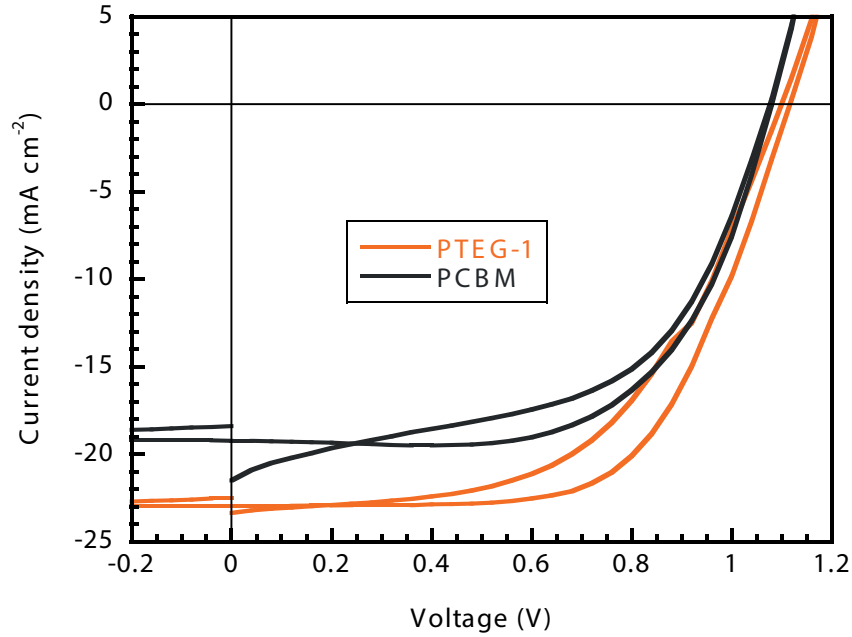


Figure 20: J-V curve of PCBM and PTEG-1 with identical FF in reverse scan.

| Device including scan direction | Voc (V) | Jsc (mA/cm ²) | FF (%) | PCE (%) |
|------------------------------------|------------|------------------------------|-----------|------------|
| PCBM reverse | 1.08 | 19.2 | 0.63 | 13.1 |
| PCBM forward | 1.08 | 21.5 | 0.52 | 12.1 |
| PTEG-1 reverse | 1.12 | 22.9 | 0.63 | 16.1 |
| PTEG-1 forward | 1.11 | 23.2 | 0.54 | 13.8 |

Table 4: Characteristics of PCBM and PTEG-1 device with an identical FF in reverse.

trap states could therefore lead to a reduction of the hysteresis.[23] Shao *et al.* have shown with photoluminescence and impedance spectroscopy, that the trap-assisted recombination at the perovskite/ETL interface is reduced significantly when using PTEG-1 over PCBM.[12] Since the hysteresis effect remains after use of PTEG-1 (in both chlorobenzene and chloroform), it can therefore not be attributed to the trap states. This statement is supported by studies that show that the trapping occurs in milliseconds, which is much faster than the hysteresis behavior that is observed.[21]

The cause of the hysteresis is most likely due to the migration of I⁻ ions.[20] I⁻ ions can arise from intrinsic defects, the degradation of MAPbI₃ by water or other polar solvents, and the non-perfect stoichiometry of the MAPbI₃ solution.[37] Under an applied bias, the I⁻ ions can drift towards the PCBM/PTEG-1 layer and cause an accumulation of charges at the interface. This accumulation subsequently

affects the band energy structure, influencing the charge extraction. Richardson *et al.* suggests that the Γ could possibly enter in between the gaps of PCBM molecules, further complicating this matter.[20]

Several extra experiments were conducted to verify the reproducibility of the J-V behavior seen in Figure 20. The statistics are displayed in separate histograms for J_{sc} , V_{oc} , FF, and PCE in Figure 21.

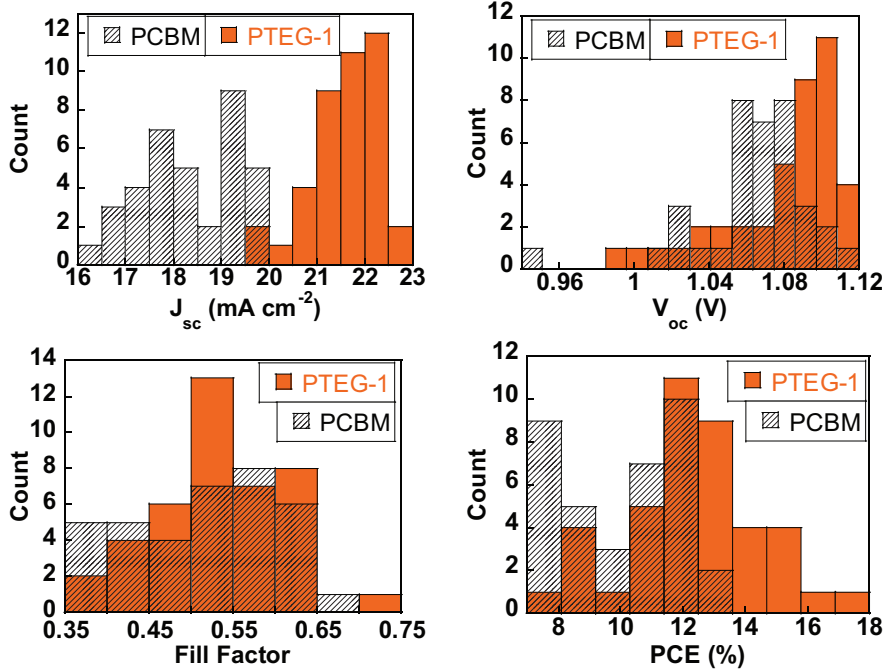


Figure 21: Histograms of J-V characteristics of PCBM and PTEG-1 devices.

The extra statistics make it evident that there is a clear trend in the case of J_{sc} : PTEG-1 performs better than PCBM, by a few mA/cm^2 . Also the V_{oc} , in the range of 1.1 V, is slightly higher on average. The higher J_{sc} can be explained by the study of Shao *et al.*, which measured a decrease in the trap-assisted recombination at the perovskite/PTEG-1 interface, compared to perovskite/PCBM.[12] Another possibility is the improved morphology at the interfaces due to PTEG-1 having a longer side-chain. Unfortunately no AFM-pictures were made to confirm this speculation.

Champion cell

The champion cell of PTEG-1 reached an efficiency of 17.7% in the reverse scan, having an uniquely high fill factor of 71%, as seen in Figure 22. This PCE is among the highest in the world for undoped nickel oxide-based perovskite solar cells with a fullerene ETL. The EQE of the device is shown in Figure 23, where an anomalous dip around 500 nm can be observed. This dip was also found in other EQE measurements, and after inspection it seems to be the result of an experimental problem at this wavelength. The champion cell,

suffers a lot from the light soaking effect, similar to the other devices. This will be discussed in the next paragraph.

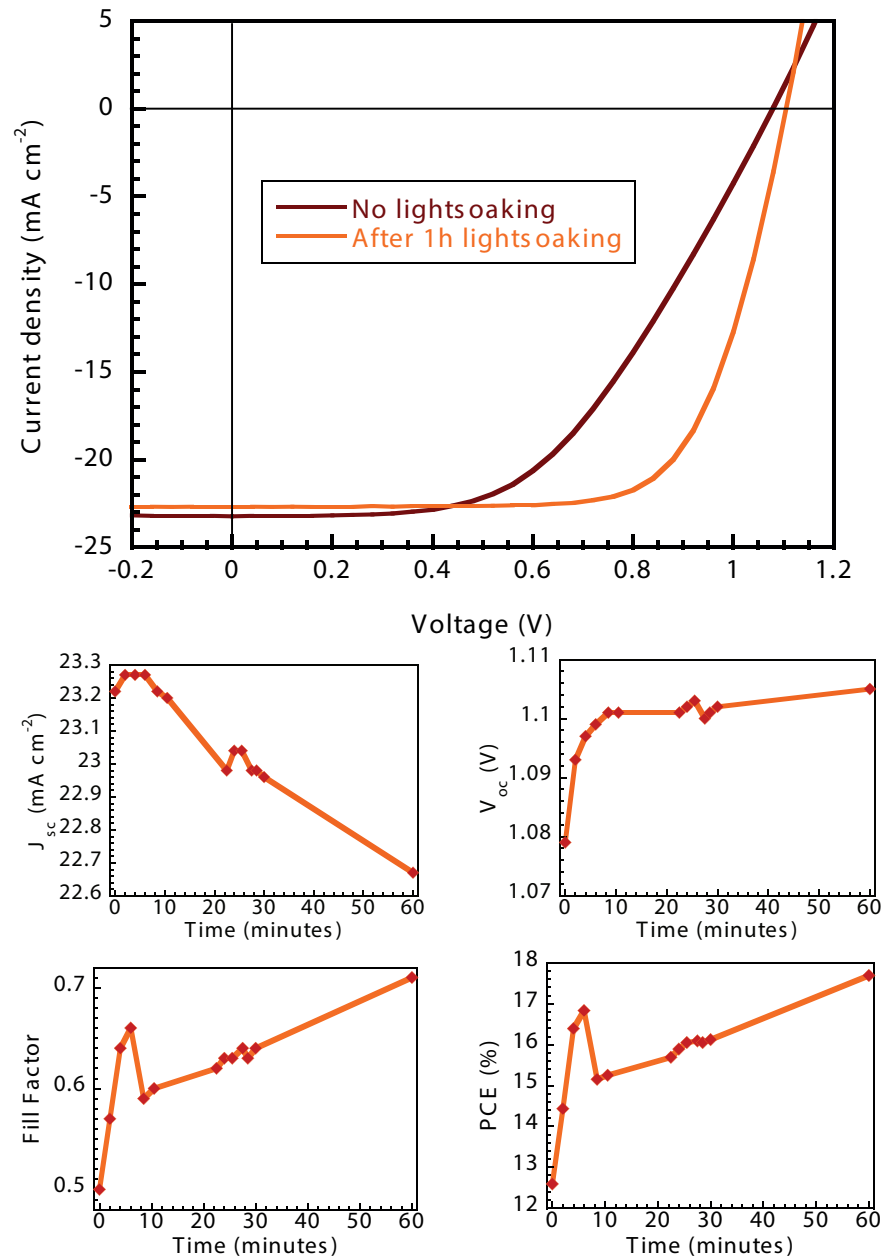


Figure 22: Light soaking effect on the reverse scan of the J-V curve of the PTEG-1 champion cell (top). The effect of light soaking on the champion cell over time (bottom).

8.3 LIGHT SOAKING

The difference in device performance of the champion cell before and after light soaking is depicted in [Figure 22](#) and [Table 5](#). Furthermore

| | Voc (V) | Jsc (mA/cm ²) | FF (%) | PCE (%) |
|--------------------------------|------------|------------------------------|-----------|------------|
| No light soaking | 1.08 | 23.2 | 0.50 | 12.6 |
| After 1+ hour light soaking | 1.11 | 22.7 | 0.71 | 17.7 |

Table 5: Light soaking of champion PTEG-1 cell over 1 hour.

the changes over time for every parameter of the device can also be seen in Figure 22.

It is unmistakable that the absolute increase of 5% in PCE can be attributed solely to the increase in fill factor from 50% to 71%: the V_{oc} might increase slightly, but is mostly canceled out by the decreasing J_{sc} . For this reason the PCE curve matches the FF curve almost completely. Zhao *et al.* suggests that charge accumulation at the interfaces might be the reason for the initially lower V_{oc} and FF. In a model they present, the photogenerated charge carriers neutralize the interfacial defects at the electrode interface, hence increasing the V_{oc} and FF.[49] Furthermore the migration of I⁻ ions, as was measured in a study by Cacovisch *et al.*[29] can influence the local built-in electrical field at the interfaces. The study mentions that the migration can account for the drop in J_{sc} .

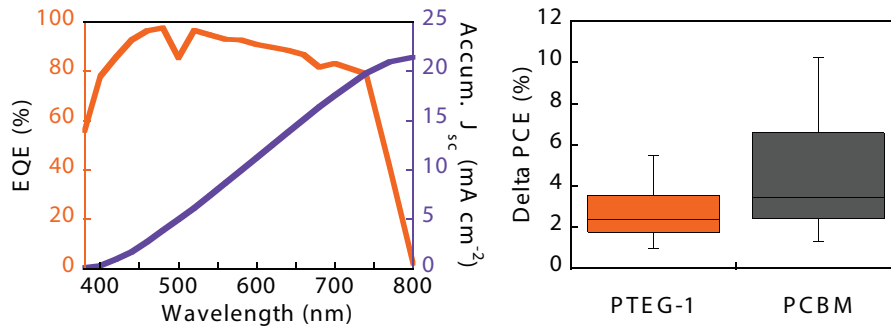


Figure 23: EQE measurement including accumulated current of the PTEG-1 champion cell (left); Absolute PCE (%) difference due to light soaking of PCBM and PTEG-1 devices (right).

Figure 23 gives an indication of the magnitude of the light soaking effect on the PCE of devices made with PTEG-1 and PCBM. When light soaking devices till the parameters stabilize (10 to 60+ minutes), the light soaking effect seems to be stronger in devices made with PCBM. Here, there are extreme cases in which the PCE increases by an absolute amount of over 10%. Although there might not be an obvious trend, it is evident that both PTEG-1 and PCBM devices suffer from the light soaking effect. This is in contrast to the study by Shao *et al.*, in which similar PTEG-1 devices were obtained with very little

to no light soaking effect.[12] After careful examination, this difference in light soaking might be due to the solvent: Shao *et al.* used chloroform instead of chlorobenzene to dissolve PTEG-1. Since the FF and the light soaking seem to be correlated [49], eliminating the light soaking effect could potentially help to solve the inconsistency of the fill factor (seen in [Figure 21](#)). The use of chloroform as a solvent for PTEG-1 will therefore be investigated in the next chapter.

ETL SOLVENT: CHLOROBENZENE VS. CHLOROFORM

The fabrication of the devices in this chapter is similar to the previous chapter, creating the structure of ITO/NiO/MAPbI₃/PTEG-1/Al. The concentration of PTEG-1 was reduced to 10 mg/ml, while the solvent was varied between chlorobenzene and chloroform.

9.1 DEVICE PERFORMANCE

The J-V characteristics of the devices made with PTEG-1 in chlorobenzene are basically identical to the ones made in chloroform: same range for J_{sc} , V_{oc} , and FF, resulting in a similar PCE. The minor reduction of the PTEG-1 concentration from 11 mg/ml to 10 mg/ml does seem to have a considerable impact on the J_{sc} , as can be seen in Figure 24. No devices that were made with the 10mg/ml concentration reached a J_{sc} of 22 mA/cm² or higher, resulting in a lower PCE compared to the 11 mg/ml batch.

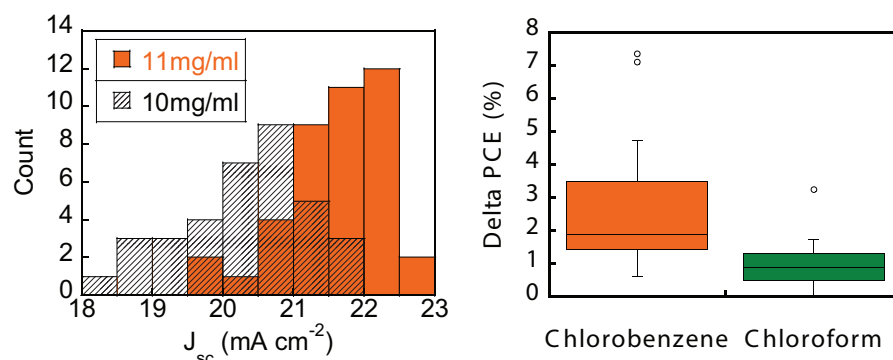


Figure 24: Difference in J_{sc} between concentrations of 10 mg/ml and 11 mg/ml PTEG-1 (left); Absolute difference in PCE (%) before and after light soaking between chlorobenzene and chloroform (right). Boxplot contains about 20 devices per solvent.

9.2 LIGHT SOAKING

Figure 24 also shows a boxplot of the absolute PCE difference of before and after light soaking of roughly 20 devices made with chlorobenzene, and 20 devices with chloroform. From this figure it becomes evident that changing the solvent from chlorobenzene to chloroform results in significantly less light soaking effect in the devices. In addition to agreeing with the study from Shao *et al.* [12], the results show

that it is not simply the ETL that changes the light soaking effect, but actually the combination of the ETL with its solvent. The reduction in light soaking effect might possibly be due to an improved morphology at the interfaces, however, no AFM-pictures were made to confirm this speculation. Reducing the light soaking effect unfortunately did not influence the FF as hoped. Although the change of FF during light soaking was reduced, the final value for the fill factor remains unchanged, varying from low to high values, similar to the statistics in [Chapter 8](#).

The light soaking effect has greatly reduced by the use of chloroform as a solvent for PTEG-1. What remains is an inconsistent FF. This inconsistency might be due to the variation in morphology of the perovskite layer: it often looks very rough. It might be possible to increase the FF by improving the morphology of the perovskite layer. An anti-solvent treatment will therefore be studied in the next chapter.

ANTI-SOLVENT TREATMENT OF MAPbI₃

Xie *et al.* added a ternary solvent to their MAPbI₃ solution, and subsequently used an anti-solvent treatment during spincoating to create uniform and low roughness perovskite films.[43] In this chapter Xie's method will be adopted in order to aim for smoother MAPbI₃ films, therefore hopefully reducing surface defects and reducing the trap-assisted recombination at the interfaces with the ETL and HTL, hence enhancing the fill factor. In addition to the solvents GBL and DMSO, the ternary solvent N-methyl-2-pyrrolidone (NMP) was added, in a volume ratio of 2:2:1. Furthermore PTEG-1 in a concentration of 10 mg/ml was used for the ETL, creating the device structure ITO/NiO/ MAPbI₃/PTEG-1/Al. Besides the addition of a ternary solvent, the spincoating was changed to a two-step program in order to incorporate the anti-solvent. Chlorobenzene is dropped onto the center of the device shortly before the end of the spincoating, washing away the MAPbI₃ solvents, hence acting as an anti-solvent.

10.1 TERNARY SOLVENT

A batch of devices was made in order to function as a control group. These devices were created using identical spincoating parameters as previous devices, and without the use of an anti-solvent. The morphology of the perovskite films with the ternary solvent looked identical to perovskite films made without NMP: rough and non-uniform. Furthermore the performance was similar, with the best device reaching a J_{sc} of 21.66 mA/cm², a V_{oc} of 1.106 V, a FF of 0.62, ultimately leading to a PCE of 14.88%.

| Recipe | 1st: v (rpm) | 1st: a (rpm/s) | 1st: t (s) | 2nd: v (rpm) | 2nd: a (rpm/s) | 2nd: t (s) |
|----------|-------------------|---------------------|-----------------|-------------------|---------------------|-----------------|
| Original | 1000 | 1000 | 10 | 7000 | 2000 | 35 |
| Slower | 1000 | 1000 | 10 | 4000 | 2000 | 30 |
| Slowest | 1000 | 1000 | 10 | 2000 | 1000 | 30 |

Table 6: Spincoating recipes for a two-step spincoating recipe with an anti-solvent treatment in the second step. Each spincoating recipe spins for 10 seconds at 1000 rpm, until it is accelerated to the second step velocity, where it remains till the end of the spincoating procedure. The symbols v , a , and t stand for velocity, acceleration and time respectively.

| Recipe | Voc (V) | Jsc (mA/cm ²) | FF (%) | PCE (%) |
|---------------------|------------|------------------------------|-----------|------------|
| Original | 0.97 | 19.2 | 0.73 | 13.6 |
| Slower & Slowest | 1.02 | 20.5 | 0.70 | 14.7 |

Table 7: Best devices made with anti-solvent treatment for the original recipe and the slower/slowest one.

10.2 ANTI-SOLVENT TREATMENT: TWO-STEP SPINCOATING

The original spincoating method by Xie *et al.* consisted out of a two-step spincoating process shown in Table 6.[43] Using this method, and applying the chlorobenzene anti-solvent ten seconds before the end of the program resulted in very smooth and uniform perovskite films. Since only a few devices were made using this exact spincoating recipe, no extensive statistics can be shown. However, a trend is noticeable: the smooth perovskite film devices dropped in J_{sc} to a value of 19.0 to 19.5 mA/cm², the V_{oc} dropped to just below 1 V, and the FF increased significantly to consistent values around 70%, with the best device reaching 73% FF, the highest in this thesis, as seen in Table 7. The thickness of the perovskite film seems to be thinner visually. A thinner perovskite layer means that less photons are absorbed, and is therefore most likely the cause of the reduced J_{sc} . The uniform and smooth perovskite film can additionally explain the increase in FF due to a decrease of trap-assisted recombination at the grain boundaries and interfaces of the perovskite.[27]

10.3 VARYING THE SPINCOATING PARAMETERS

In order to maintain the high FF while increasing the J_{sc} to its original value, it was decided to slightly change the spincoating parameters. By slowing down the second spincoating step, it could either lead to a thicker MAPBI₃ layer, or reduce the possible damage done by the anti-solvent. This should hopefully increase the J_{sc} and V_{oc} . Multiple spincoating speeds for the second step were therefore examined, as shown in Table 6. Since only very little devices were made with each new spincoating recipe, no definite conclusion can be drawn concerning the difference between the device performance of these new recipes. On the other hand, the differences with the 7000 rpm spincoating recipe are apparent (Table 7): the J_{sc} increased back to 21 mA/cm², while the V_{oc} reached values of around 1.05 V. The FF was reduced slightly compared to the 7000 rpm, but was on average still higher than the devices prepared without anti-solvent: multiple devices reached a FF of 66% and one with 70%. Visually the perovskite

films were not as smooth and uniform as the 7000 rpm batch, although an improvement was still observable. Due to time restrictions the experiment was discontinued, and no further optimizations were accomplished. From these experiments it is likely that the anti-solvent treatment can increase the fill factor and its reproducibility, and with further adjusting could lead to highly reproducible solar cells with efficiencies of over 15%.

CONCLUSIONS AND OUTLOOK

The influence and necessity of the scrubbing of the ITO anodic contacts was discussed in a qualitative experiment. Cleaned and non-scrubbed ITO peaks are roughly 20 to 30 nm in height, measured from the lowest to the highest point on the surface. Scrubbing the ITO surface by hand can result in a reduction of the high ITO peaks, smoothing the overall morphology and reducing the height by several nanometers. Depending on the hardness of the scrubbing material, and the force applied, the surface can become damaged. This resulted in unwanted scratches when using diamond lapping paper and steel wool. Without making large batches of devices it is difficult to say whether the scrubbing influences the device performance, since it depends on the thickness of the spincoated NiO layer.

Optimizing the NiO layer could help improve the device performance, mainly through the FF. Therefore three different precursors for the NiO layer were explored: nickel(II) acetate tetrahydrate, nickel(II) nitrate hexahydrate, and nickel(II) formate dihydrate. The surface of the nickel(II) nitrate hexahydrate was covered with large particles in the range of 0.3 to 5 micrometers, likely due to precipitation of the salt before spincoating. After annealing at 300°C, the NiO layer is very hard, which made it impossible to measure the thickness with the Dektak. Ellipsometer and X-ray reflectivity measurements allowed for thickness measurements, but were not always consistent. The NiO layers made with 0.5 M of nickel(II) formate have a thickness of roughly 8 nm according to the XRR and ellipsometry data. Contrasting data is also seen from the ellipsometer measurement on low iron glass, giving a thickness that is more than double: 19 nm. Additional data from the XRR-setup shows that a doubling in the concentration from 0.5 M to 1 M seems to roughly double the thickness of the layer in the case of nickel(II) formate. No other conclusive arguments can be given, since data and statistics are lacking.

Numerous perovskite solar cells were investigated with an active layer of MAPbI₃ and a HTL of NiO. The ETL materials were varied, as were the solvents used to process them. The fullerene derivatives PCBM and PTEG-1 were compared, dissolved in both chlorobenzene and chloroform. Overall the devices made with PTEG-1 achieved about 3% higher efficiencies, with the champion cell reaching 17.7% PCE. The change of ETL from PCBM to PTEG-1, dissolved in chlorobenzene, resulted in a J_{sc} of up to 23 mA/cm², an increase of nearly 3

mA/cm^2 , while further slightly improving the V_{oc} from 1.05 V to 1.1 V. The increase of J_{sc} and V_{oc} can possibly be explained by the reduction of trap-assisted recombination at the perovskite-ETL interface. Another possibility is the improved morphology at the perovskite/ETL interface due to PTEG-1 having a longer side-chain. Unfortunately no AFM-pictures were made to confirm this speculation. Both device structures suffered a lot from the light soaking effect, which can be attributed to ionic migration, trap-assisted recombination, or a combination hereof. Furthermore, the devices showed inconsistent fill factors, reaching anywhere from 35% to 70%.

The use of PTEG-1 in combination with a change of solvent to chloroform, resulted in a significant reduction of the light soaking effect, removing the instability of the fill factor during exposure to light. The inconsistency of the fill factor between devices remains, however. In addition it was noticed that devices made with 10 mg/ml PTEG-1 on average have a 1 mA/cm^2 lower J_{sc} than devices made with 11 mg/ml PTEG-1, never reaching 22 mA/cm^2 . This statement is not indisputable, since the sample size might not be large enough.

To remove the inconsistency and improve the fill factor, an experiment with a ternary perovskite solvent and anti-solvent treatment was investigated. The morphology of the perovskite improved considerably, likely reducing the defect density and therefore trap-assisted recombination at the interfaces. This subsequently resulted in better fill factors of up to 73%, the highest in this thesis. A faster two-step spincoating program was used for the anti-solvent treatment, which resulted in thinner perovskite films, and therefore lower J_{sc} . Decreasing the speed while including the anti-solvent resulted in better J_{sc} 's up to 21 mA/cm^2 , while reaching FF's of 66% and higher. This fill factor is higher than the average of the devices made without anti-solvent treatment.

Outlook

Future research could focus on doping the NiO layer, allowing for a higher hole conductivity and PCE. This would require the best NiO precursors, optimized in thickness. Optimization might be difficult however, since thickness measurements of NiO layers are challenging. The work on anti-solvent treatment has also shown to help improve the FF. Optimizing the two-step spincoating process can allow for further improvement of the FF and its reproducibility. This can possibly eliminate the last remaining inconsistency concerning the J-V characteristics of this type of device. This would allow for consistent production of solar cells with efficiencies of over 15% PCE.

An improvement of the production process of the device fabrication can also be imagined. Reducing or removing the scrubbing pro-

cess all together could save up to an hour per experiment. Furthermore stability tests with NiO layers could be performed. If the NiO layers are stable for longer periods of time, it could be possible to fabricate big batches of NiO samples and store them for later use. This would save time during the preparation for an experiment. This could result in a higher experimental output, and therefore increase the productivity of a scientist studying these solar cells.

BIBLIOGRAPHY

- [1] IEA. "Key World Energy Statistics." In: (2016). URL: <https://www.iea.org/publications/freepublications/publication/KeyWorld2016.pdf>.
- [2] Peter M. Cox, Richard A. Betts, Chris D. Jones, Steven A. Spall, and Ian J. Totterdell. "Acceleration of global warming due to carbon-cycle feedbacks in a coupled climate model." In: *Nature* 408.6809 (2000), pp. 184–187. ISSN: 0028-0836. DOI: [10.1038/35041539](https://doi.org/10.1038/35041539). URL: <http://dx.doi.org/10.1038/35041539>.
- [3] Martin A. Green, Keith Emery, Yoshihiro Hishikawa, Wilhelm Warta, Ewan D. Dunlop, Dean H. Levi, and Anita W. Y. Ho-Baillie. "Solar cell efficiency tables (version 49)." In: *Progress in Photovoltaics: Research and Applications* 25.1 (2017). PIP-16-252, pp. 3–13. ISSN: 1099-159X. DOI: [10.1002/pip.2855](https://doi.org/10.1002/pip.2855). URL: <http://dx.doi.org/10.1002/pip.2855>.
- [4] Michael Saliba et al. "Incorporation of rubidium cations into perovskite solar cells improves photovoltaic performance." In: *Science* 354.6309 (2016), pp. 206–209. ISSN: 0036-8075. DOI: [10.1126/science.aah5557](https://doi.org/10.1126/science.aah5557). eprint: <http://science.sciencemag.org/content/354/6309/206.full.pdf>. URL: <http://science.sciencemag.org/content/354/6309/206>.
- [5] Stefaan De Wolf, Jakub Holovsky, Soo-Jin Moon, Philipp Löper, Bjoern Niesen, Martin Ledinsky, Franz-Josef Haug, Jun-Ho Yum, and Christophe Ballif. "Organometallic Halide Perovskites: Sharp Optical Absorption Edge and Its Relation to Photovoltaic Performance." In: *The Journal of Physical Chemistry Letters* 5.6 (2014). PMID: 26270984, pp. 1035–1039. DOI: [10.1021/jz500279b](https://doi.org/10.1021/jz500279b). eprint: <http://dx.doi.org/10.1021/jz500279b>. URL: <http://dx.doi.org/10.1021/jz500279b>.
- [6] Giles E. Eperon, Samuel D. Stranks, Christopher Menelaou, Michael B. Johnston, Laura M. Herz, and Henry J. Snaith. "Formamidinium lead trihalide: a broadly tunable perovskite for efficient planar heterojunction solar cells." In: *Energy Environ. Sci.* 7 (3 2014), pp. 982–988. DOI: [10.1039/C3EE43822H](https://doi.org/10.1039/C3EE43822H). URL: <http://dx.doi.org/10.1039/C3EE43822H>.
- [7] Zhaoning Song, Suneth C. Watthage, Adam B. Phillips, and Michael J. Heben. "Pathways toward high-performance perovskite solar cells: review of recent advances in organo-metal halide perovskites for photovoltaic applications." In: *Journal of Photonics for Energy* 6.2 (2016), p. 022001. DOI: [10.1117/1.JPE.6.022001](https://doi.org/10.1117/1.JPE.6.022001). URL: <http://dx.doi.org/10.1117/1.JPE.6.022001>.

- [8] K. Xerxes Steirer et al. "Enhanced Efficiency in Plastic Solar Cells via Energy Matched Solution Processed NiO_x Interlayers." In: *Advanced Energy Materials* 1.5 (2011), pp. 813–820. ISSN: 1614-6840. DOI: [10.1002/aenm.201100234](https://doi.org/10.1002/aenm.201100234). URL: <http://dx.doi.org/10.1002/aenm.201100234>.
- [9] Peng Gao, Michael Gratzel, and Mohammad K. Nazeeruddin. "Organohalide lead perovskites for photovoltaic applications." In: *Energy Environ. Sci.* 7 (8 2014), pp. 2448–2463. DOI: [10.1039/C4EE00942H](https://doi.org/10.1039/C4EE00942H). URL: <http://dx.doi.org/10.1039/C4EE00942H>.
- [10] P. S. Whitfield, N. Herron, W. E. Guise, K. Page, Y. Q. Cheng, I. Milas, and M. K. Crawford. "Structures, Phase Transitions and Tricritical Behavior of the Hybrid Perovskite Methyl Ammonium Lead Iodide." In: *Scientific Reports* 6 (2016). Article, 35685 EP –. URL: <http://dx.doi.org/10.1038/srep35685>.
- [11] Krzysztof Galkowski et al. "Determination of the exciton binding energy and effective masses for methylammonium and formamidinium lead tri-halide perovskite semiconductors." In: *Energy Environ. Sci.* 9 (3 2016), pp. 962–970. DOI: [10.1039/C5EE03435C](https://doi.org/10.1039/C5EE03435C). URL: <http://dx.doi.org/10.1039/C5EE03435C>.
- [12] Shuyan Shao et al. "Elimination of the light soaking effect and performance enhancement in perovskite solar cells using a fullerene derivative." In: *Energy Environ. Sci.* 9 (7 2016), pp. 2444–2452. DOI: [10.1039/C6EE01337F](https://doi.org/10.1039/C6EE01337F). URL: <http://dx.doi.org/10.1039/C6EE01337F>.
- [13] S.M. Sze. *Semiconductor devices, physics and technology*. Wiley, 1985. URL: <https://books.google.nl/books?id=gb0QAQAAMAJ>.
- [14] Inductiveload. "Analogue Electronics/pn Junctions." In: (2007). URL: https://en.wikibooks.org/wiki/Analogue_Electronics/pn_Junctions.
- [15] Wahyudi Purnomo Harry Sudiby Purnomo Sidi Priambodo Didik Sukoco and Djoko Hartanto. "Electric Energy Management and Engineering in Solar Cell System." In: (unknown). URL: <https://www.intechopen.com/books/solar-cells-research-and-application-perspectives/electric-energy-management-and-engineering-in-solar-cell-system>.
- [16] B.G.H.M. Groeneveld. "POLYMER – NANOCRYSTAL TANDEM SOLAR CELLS FOR ENHANCED POWER CONVERSION EFFICIENCIES." In: (2015).
- [17] University of Liverpool Jon Mayor. "Lecture 6 Junction characterisation." In: (Nov 6th, 2014). URL: <https://www.slideshare.net/RobertTreharne/lecture-6-junction-characterisation>.

- [18] William Shockley and Hans J. Queisser. "Detailed Balance Limit of Efficiency of p-n Junction Solar Cells." In: *Journal of Applied Physics* 32.3 (1961), pp. 510–519. DOI: [10.1063/1.1736034](https://doi.org/10.1063/1.1736034). eprint: <http://dx.doi.org/10.1063/1.1736034>. URL: <http://dx.doi.org/10.1063/1.1736034>.
- [19] C.A. Gueymard, D. Myers, and K. Emery. "Proposed reference irradiance spectra for solar energy systems testing." In: *Solar Energy* 73.6 (2002), pp. 443–467. ISSN: 0038-092X. DOI: [https://doi.org/10.1016/S0038-092X\(03\)00005-7](https://doi.org/10.1016/S0038-092X(03)00005-7). URL: <http://www.sciencedirect.com/science/article/pii/S0038092X03000057>.
- [20] Giles Richardson, Simon E. J. O’Kane, Ralf G. Niemann, Timo A. Peltola, Jamie M. Foster, Petra J. Cameron, and Alison B. Walker. "Can slow-moving ions explain hysteresis in the current-voltage curves of perovskite solar cells?" In: *Energy Environ. Sci.* 9 (4 2016), pp. 1476–1485. DOI: [10.1039/C5EE02740C](https://doi.org/10.1039/C5EE02740C). URL: <http://dx.doi.org/10.1039/C5EE02740C>.
- [21] Bo Chen, Mengjin Yang, Shashank Priya, and Kai Zhu. "Origin of J–V Hysteresis in Perovskite Solar Cells." In: *The Journal of Physical Chemistry Letters* 7.5 (2016). PMID: 26886052, pp. 905–917. DOI: [10.1021/acs.jpcllett.6b00215](https://doi.org/10.1021/acs.jpcllett.6b00215). eprint: <http://dx.doi.org/10.1021/acs.jpcllett.6b00215>. URL: <http://dx.doi.org/10.1021/acs.jpcllett.6b00215>.
- [22] Henry J. Snaith, Antonio Abate, James M. Ball, Giles E. Eperon, Tomas Leijtens, Nakita K. Noel, Samuel D. Stranks, Jacob Tse-Wei Wang, Konrad Wojciechowski, and Wei Zhang. "Anomalous Hysteresis in Perovskite Solar Cells." In: *The Journal of Physical Chemistry Letters* 5.9 (2014). PMID: 26270088, pp. 1511–1515. DOI: [10.1021/jz500113x](https://doi.org/10.1021/jz500113x). eprint: <http://dx.doi.org/10.1021/jz500113x>. URL: <http://dx.doi.org/10.1021/jz500113x>.
- [23] Konrad Wojciechowski et al. "Heterojunction Modification for Highly Efficient Organic–Inorganic Perovskite Solar Cells." In: *ACS Nano* 8.12 (2014). PMID: 25415931, pp. 12701–12709. DOI: [10.1021/nn505723h](https://doi.org/10.1021/nn505723h). eprint: <http://dx.doi.org/10.1021/nn505723h>. URL: <http://dx.doi.org/10.1021/nn505723h>.
- [24] Jixian Xu et al. "Perovskite fullerene hybrid materials suppress hysteresis in planar diodes." In: *Nature Communications* 6 (2015). Article, 7081 EP –. URL: <http://dx.doi.org/10.1038/ncomms8081>.
- [25] Stephan van Reenen, Martijn Kemerink, and Henry J. Snaith. "Modeling Anomalous Hysteresis in Perovskite Solar Cells." In: *The Journal of Physical Chemistry Letters* 6.19 (2015). PMID: 26722875, pp. 3808–3814. DOI: [10.1021/acs.jpcllett.5b01645](https://doi.org/10.1021/acs.jpcllett.5b01645). eprint: <http://dx.doi.org/10.1021/acs.jpcllett.5b01645>. URL: <http://dx.doi.org/10.1021/acs.jpcllett.5b01645>.

- [26] J. Beilsten-Edmands, G. E. Eperon, R. D. Johnson, H. J. Snaith, and P. G. Radaelli. "Non-ferroelectric nature of the conductance hysteresis in $\text{CH}_3\text{NH}_3\text{PbI}_3$ perovskite-based photovoltaic devices." In: *Applied Physics Letters* 106.17 (2015), p. 173502. DOI: [10.1063/1.4919109](https://doi.org/10.1063/1.4919109). eprint: <http://dx.doi.org/10.1063/1.4919109>. URL: <http://dx.doi.org/10.1063/1.4919109>.
- [27] Shuyan Shao, Mustapha Abdu-Aguye, Tejas S. Sherkar, Hong-Hua Fang, Sampson Adjokatse, Gert ten Brink, Bart J. Kooi, L. Jan Anton Koster, and Maria Antonietta Loi. "The Effect of the Microstructure on Trap-Assisted Recombination and Light Soaking Phenomenon in Hybrid Perovskite Solar Cells." In: *Advanced Functional Materials* 26.44 (2016), pp. 8094–8102. ISSN: 1616-3028. DOI: [10.1002/adfm.201602519](https://doi.org/10.1002/adfm.201602519). URL: <http://dx.doi.org/10.1002/adfm.201602519>.
- [28] Dane W. deQuilettes, Wei Zhang, Victor M. Burlakov, Daniel J. Graham, Tomas Leijtens, Anna Osherov, Vladimir Bulovic, Henry J. Snaith, David S. Ginger, and Samuel D. Stranks. "Photo-induced halide redistribution in organic-inorganic perovskite films." In: *Nature Communications* 7 (2016). Article, 11683 EP -. URL: <http://dx.doi.org/10.1038/ncomms11683>.
- [29] S. Cacovich, L. Cina, F. Matteocci, G. Divitini, P. A. Midgley, A. Di Carlo, and C. Ducati. "Gold and iodine diffusion in large area perovskite solar cells under illumination." In: *Nanoscale* 9 (14 2017), pp. 4700–4706. DOI: [10.1039/C7NR00784A](https://doi.org/10.1039/C7NR00784A). URL: <http://dx.doi.org/10.1039/C7NR00784A>.
- [30] Kiyoshi Sugiyama, Hisao Ishii, Yukio Ouchi, and Kazuhiko Seki. "Dependence of indium–tin–oxide work function on surface cleaning method as studied by ultraviolet and x-ray photoemission spectroscopies." In: *Journal of Applied Physics* 87.1 (2000), pp. 295–298. DOI: [10.1063/1.371859](https://doi.org/10.1063/1.371859). eprint: <http://dx.doi.org/10.1063/1.371859>. URL: <http://dx.doi.org/10.1063/1.371859>.
- [31] K. X. Steirer et al. "Nickel oxide interlayer films from nickel formate-ethylenediamine precursor: influence of annealing on thin film properties and photovoltaic device performance." In: *J. Mater. Chem. A* 3 (20 2015), pp. 10949–10958. DOI: [10.1039/C5TA01379H](https://doi.org/10.1039/C5TA01379H). URL: <http://dx.doi.org/10.1039/C5TA01379H>.
- [32] Ze Yu and Licheng Sun. "Recent Progress on Hole-Transporting Materials for Emerging Organometal Halide Perovskite Solar Cells." In: *Advanced Energy Materials* 5.12 (2015). 1500213, 1500213–n/a. ISSN: 1614-6840. DOI: [10.1002/aenm.201500213](https://doi.org/10.1002/aenm.201500213). URL: <http://dx.doi.org/10.1002/aenm.201500213>.
- [33] Samuel D. Stranks, Giles E. Eperon, Giulia Grancini, Christopher Menelaou, Marcelo J. P. Alcocer, Tomas Leijtens, Laura M. Herz, Annamaria Petrozza, and Henry J. Snaith. "Electron-Hole Diffusion Lengths Exceeding 1 Micrometer in an Organometal

- Trihalide Perovskite Absorber." In: *Science* 342.6156 (2013), pp. 341–344. ISSN: 0036-8075. DOI: [10.1126/science.1243982](https://doi.org/10.1126/science.1243982). eprint: <http://science.sciencemag.org/content/342/6156/341.full.pdf>. URL: <http://science.sciencemag.org/content/342/6156/341>.
- [34] Qianqian Lin, Ardalan Armin, Ravi Chandra Raju Nagiri, Paul L. Burn, and Paul Meredith. "Electro-optics of perovskite solar cells." In: *Nat Photon* 9.2 (2015). Article, pp. 106–112. ISSN: 1749-4885. URL: <http://dx.doi.org/10.1038/nphoton.2014.284>.
- [35] Nicholas Aristidou, Irene Sanchez-Molina, Thana Chotchuangchutchaval, Michael Brown, Luis Martinez, Thomas Rath, and Saif A. Haque. "The Role of Oxygen in the Degradation of Methylammonium Lead Trihalide Perovskite Photoactive Layers." In: *Angewandte Chemie International Edition* 54.28 (2015), pp. 8208–8212. ISSN: 1521-3773. DOI: [10.1002/anie.201503153](https://doi.org/10.1002/anie.201503153). URL: <http://dx.doi.org/10.1002/anie.201503153>.
- [36] Hui-Seon Kim et al. "Lead Iodide Perovskite Sensitized All-Solid-State Submicron Thin Film Mesoscopic Solar Cell with Efficiency Exceeding 9%." In: *Scientific Reports* 2 (2012). Article, 591 EP –. URL: <http://dx.doi.org/10.1038/srep00591>.
- [37] Tomas Leijtens, Giles E. Eperon, Nakita K. Noel, Severin N. Habisreutinger, Annamaria Petrozza, and Henry J. Snaith. "Stability of Metal Halide Perovskite Solar Cells." In: *Advanced Energy Materials* 5.20 (2015). 1500963, 1500963–n/a. ISSN: 1614-6840. DOI: [10.1002/aenm.201500963](https://doi.org/10.1002/aenm.201500963). URL: <http://dx.doi.org/10.1002/aenm.201500963>.
- [38] Aurélien M. A. Leguy et al. "Reversible Hydration of CH₃NH₃PbI₃ in Films, Single Crystals, and Solar Cells." In: *Chemistry of Materials* 27.9 (2015), pp. 3397–3407. DOI: [10.1021/acs.chemmater.5b00660](https://doi.org/10.1021/acs.chemmater.5b00660). eprint: <http://dx.doi.org/10.1021/acs.chemmater.5b00660>. URL: <http://dx.doi.org/10.1021/acs.chemmater.5b00660>.
- [39] Thomas D. Anthopoulos, Dago M. de Leeuw, Eugenio Cantatore, Patrick van 't Hof, Jan Alma, and Jan C. Hummelen. "Solution processible organic transistors and circuits based on a C₇₀ methanofullerene." In: *Journal of Applied Physics* 98.5 (2005), p. 054503. DOI: [10.1063/1.2034083](https://doi.org/10.1063/1.2034083). eprint: <http://dx.doi.org/10.1063/1.2034083>. URL: <http://dx.doi.org/10.1063/1.2034083>.
- [40] L. J. A. Koster, V. D. Mihailetschi, and P. W. M. Blom. "Ultimate efficiency of polymer/fullerene bulk heterojunction solar cells." In: *Applied Physics Letters* 88.9 (2006), p. 093511. DOI: [10.1063/1.2181635](https://doi.org/10.1063/1.2181635). eprint: <http://dx.doi.org/10.1063/1.2181635>. URL: <http://dx.doi.org/10.1063/1.2181635>.

- [41] Andres Garcia, Gregory C. Welch, Erin L. Ratcliff, David S. Ginley, Guillermo C. Bazan, and Dana C. Olson. "Improvement of Interfacial Contacts for New Small-Molecule Bulk-Heterojunction Organic Photovoltaics." In: *Advanced Materials* 24.39 (2012), pp. 5368–5373. ISSN: 1521-4095. DOI: [10.1002/adma.201200963](https://doi.org/10.1002/adma.201200963). URL: <http://dx.doi.org/10.1002/adma.201200963>.
- [42] Nam Joong Jeon, Jun Hong Noh, Young Chan Kim, Woon Seok Yang, Seungchan Ryu, and Sang Il Seok. "Solvent engineering for high performance inorganic organic hybrid perovskite solar cells." In: *Nat Mater* 13.9 (2014). Article, pp. 897–903. ISSN: 1476-1122. URL: <http://dx.doi.org/10.1038/nmat4014>.
- [43] Lin Xie, Heewon Hwang, Minjung Kim, and Kyungkon Kim. "Ternary solvent for $\text{CH}_3\text{NH}_3\text{PbI}_3$ perovskite films with uniform domain size." In: *Phys. Chem. Chem. Phys.* 19 (2 2017), pp. 1143–1150. DOI: [10.1039/C6CP06709C](https://doi.org/10.1039/C6CP06709C). URL: <http://dx.doi.org/10.1039/C6CP06709C>.
- [44] Emilio J. Juarez-Perez, Zafer Hawash, Sonia R. Raga, Luis K. Ono, and Yabing Qi. "Thermal degradation of $\text{CH}_3\text{NH}_3\text{PbI}_3$ perovskite into NH_3 and CH_3I gases observed by coupled thermogravimetry-mass spectrometry analysis." In: *Energy Environ. Sci.* 9 (11 2016), pp. 3406–3410. DOI: [10.1039/C6EE02016J](https://doi.org/10.1039/C6EE02016J). URL: <http://dx.doi.org/10.1039/C6EE02016J>.
- [45] Mario Birkholz. "Grazing Incidence Configurations." In: (2006), pp. 143–182. URL: <http://dx.doi.org/10.1002/3527607595.ch4>.
- [46] Dr. Graeme Blake. "Lecture from course Characterisation of Materials: X-ray Diffraction, part 4. University of Groningen course." In: (2016).
- [47] J.A. Woollam. "Information retrieved from the website of the manufacturer May 2017." In: (). URL: <https://www.jawoollam.com/resources/ellipsometry-tutorial/thin-film-thickness>.
- [48] Yuanyuan Zhou, Zhongmin Zhou, Min Chen, Yingxia Zong, Jinsong Huang, Shuping Pang, and Nitin P. Padture. "Doping and alloying for improved perovskite solar cells." In: *J. Mater. Chem. A* 4 (45 2016), pp. 17623–17635. DOI: [10.1039/C6TA08699C](https://doi.org/10.1039/C6TA08699C). URL: <http://dx.doi.org/10.1039/C6TA08699C>.
- [49] Chen Zhao, Bingbing Chen, Xianfeng Qiao, Lin Luan, Kai Lu, and Bin Hu. "Revealing Underlying Processes Involved in Light Soaking Effects and Hysteresis Phenomena in Perovskite Solar Cells." In: *Advanced Energy Materials* 5.14 (2015). 1500279, 1500279–n/a. ISSN: 1614-6840. DOI: [10.1002/aenm.201500279](https://doi.org/10.1002/aenm.201500279). URL: <http://dx.doi.org/10.1002/aenm.201500279>.